

1

2

3

4

# Cosmic ray validation of electrode positions in small-strip thin gap chambers for the upgrade of the ATLAS detector

5

Lia Formenti

6

7

8

Department of Physics  
McGill University, Montreal  
October, 2021

9

10

11

12

13

A thesis submitted to  
McGill University  
in partial fulfillment of the  
requirements of the degree of  
Master of Science

# <sup>15</sup> Table of Contents

<sup>16</sup>	<b>1</b>	<b>Introduction</b>	<b>1</b>
<sup>17</sup>	<b>2</b>	<b>High energy particle physics</b>	<b>4</b>
<sup>18</sup>	2.1	The Standard Model . . . . .	4
<sup>19</sup>	2.2	Beyond the Standard Model . . . . .	6
<sup>20</sup>	2.3	Studying high energy particle physics with accelerators . . . . .	7
<sup>21</sup>	<b>3</b>	<b>The LHC and the ATLAS experiment</b>	<b>9</b>
<sup>22</sup>	3.1	The Large Hadron Collider . . . . .	9
<sup>23</sup>	3.2	The High-Luminosity LHC . . . . .	10
<sup>24</sup>	3.3	The ATLAS experiment . . . . .	12
<sup>25</sup>	<b>4</b>	<b>The New Small Wheels</b>	<b>17</b>
<sup>26</sup>	4.1	Motivation for the New Small Wheels . . . . .	17
<sup>27</sup>	4.2	Design of the NSWs . . . . .	20
<sup>28</sup>	4.3	Small-strip thin gap chambers . . . . .	20
<sup>29</sup>	4.4	sTGC Quadruplet Construction . . . . .	23
<sup>30</sup>	4.5	NSW alignment . . . . .	24
<sup>31</sup>	<b>5</b>	<b>Using cosmic muons to measure relative strip position offsets</b>	<b>27</b>
<sup>32</sup>	5.1	Cosmic rays . . . . .	27
<sup>33</sup>	5.2	Experimental setup . . . . .	28

34	5.3 Data acquisition . . . . .	29
35	5.4 Data preparation . . . . .	30
36	5.4.1 Data quality cuts on electrode hits . . . . .	30
37	5.4.2 Clustering and tracking . . . . .	30
38	5.5 Relative local offsets . . . . .	32
39	5.6 Systematic uncertainty . . . . .	38
40	5.7 Discussion . . . . .	39
41	<b>6 Using x-rays to measure relative strip position offsets</b>	<b>41</b>
42	6.1 Experimental setup . . . . .	41
43	6.2 Data acquisition . . . . .	43
44	6.3 Data preparation . . . . .	43
45	6.4 Measuring local offsets . . . . .	43
46	6.5 Measuring relative local offsets . . . . .	45
47	<b>7 Comparing cosmic muon and x-ray relative strip position offsets</b>	<b>48</b>
48	7.1 Results . . . . .	48
49	7.2 Discussion . . . . .	53
50	7.3 Next steps . . . . .	54
51	<b>8 Summary and outlook</b>	<b>56</b>
52	<b>References</b>	<b>57</b>
53	<b>APPENDICES</b>	<b>64</b>
54	<b>A Cluster position uncertainty</b>	<b>65</b>
55	<b>B Analysis statistics</b>	<b>67</b>

56	<b>C Analysis systematics</b>	<b>69</b>
57	C.1 Residual distribution fit function	69
58	C.2 Cosmic muon data collection voltage	72
59	C.3 Cluster fit algorithm	73
60	C.4 Differential non-linearity	74
61	<b>D Printable plots</b>	<b>77</b>

## Abstract

63 The Large Hadron Collider (LHC) is used to generate subatomic physics processes at the  
64 energy frontier to challenge our understanding of the Standard Model of particle physics.  
65 The particle collision rate at the LHC will be increased up to seven times its design value in  
66 2025-2027 by an extensive upgrade program. The innermost endcaps of the ATLAS muon  
67 spectrometer consist of two wheels of muon detectors that must be replaced to maintain  
68 the muon momentum resolution in the high-rate environment. The so-called New Small  
69 Wheels (NSWs) are made of two detector technologies: micromegas and small-strip thin gap  
70 chambers (sTGCs). The sTGCs are gas ionization chambers that hold a thin volume of gas  
71 between two cathode boards. One board is segmented into copper readout strips of 3.2 mm  
72 pitch that are used to precisely reconstruct the coordinate of a passing muon. Modules of  
73 four sTGCs glued together into quadruplets cover the NSWs. Quadruplets were designed  
74 to achieve a 1 mrad angular resolution to fulfill the spectrometer's triggering and precision  
75 tracking requirements. To achieve the required angular resolution the absolute position of  
76 the readout strips must be known in the ATLAS coordinate system to within 100  $\mu\text{m}$ . At  
77 McGill University, the performance of sTGC quadruplets was characterized using cosmic ray  
78 data before being sent to CERN, where the charge profile left by x-rays is used to measure  
79 the offset of the strip patterns with respect to nominal at a limited number of points on  
80 the surface of each quadruplet. The x-ray strip position measurements have acceptable but  
81 limited precision and do not span the whole area of the strip layers. Given the importance of  
82 knowing the absolute position of each readout strip to achieve the performance requirements  
83 of the NSWs, the x-ray method must be validated by an independent method. Cosmic ray  
84 data is used to characterize the relative alignment between layers and validate the x-ray  
85 method.

## Résumé

Le grand collisionneur des hadrons (LHC) utilise des collisions de protons afin de générer des processus de la physique subatomique à la frontière même de la haute énergie, et ceci afin de tenter remettre en cause le modèle standard de la physique des particules. Le taux des collisions entre protons au LHC sera augmenté jusqu'à sept fois le taux nominal d'ici 2025-2027 à l'aide d'un programme de mise à niveau de grande envergure. Une partie du spectromètre à muons du détecteur ATLAS consistant de deux roues de détecteurs de muons doit être remplacée afin de maintenir la résolution sur l'inertie des muons à haut taux de collision. Appelées les Nouvelles Petites Roues (NSWs), elles utilisent deux technologies de détection différentes: des chambres micromegas et des chambres à petites bandes et à intervalles fins (sTGCs). Les sTGCs sont des chambres d'ionisation de gaz, qui contiennent un volume très fin de gaz entre deux panneaux cathodiques. Un panneau est segmenté avec de petites bandes en cuivre en pente de 3.2 mm. Ceux-ci détectent le signal laissé par des muons et permettent la mesure précise des coordonnées spatiales des muons qui traversent le détecteur. Des modules de quatre sTGCs collés ensemble en quaduplets couvrent la superficie des NSWs. Ces quadruplets ont été conçus afin de permettre une résolution angulaire de 1 mrad, et de satisfaire les exigences des systèmes de déclenchement et de mesures de précision. Afin d'atteindre cette résolution angulaire il faut que la position absolue de chaque bande soit connue au sein du détecteur ATLAS avec une précision d'au moins 100  $\mu$ m. À l'Université de McGill, la performance des quadruplets a été caractériser avec des rayons cosmiques avant leur envoi au CERN, où le profil des charges laissé par des rayons X est utilisé pour mesurer le déplacement du motif des bandes par rapport à leur emplacement nominal. Ceci est fait à un nombre de positions limité sur la surface des quadruplets. Ces déplacements, mesurés par les rayons X, ont une précision acceptable mais limitée et ne couvrent pas la région entière des panneaux. Étant donné l'importance de la caractérisation précise de la position absolue de chaque bande afin de réaliser les exigences de rendement des NSWs, une méthode indépendante de validation de la méthode des rayons X est requise. Les données recueillies avec les rayons cosmiques sont utilisées pour caractériser l'alignement relatif entre les panneaux et valider la méthode des rayons-X.

## Acknowledgements

- 116 Experimental particle physics projects are never done alone. I am grateful to have been  
117 working with the ATLAS Collaboration for two years now.
- 118 Thank you to Dr. Brigitte Vachon for her guidance throughout this project and for editing  
119 this thesis. I am consistently amazed by her ability to jump into the details of my project  
120 and discuss them with me.
- 121 Thanks also to Dr. Benoit Lefebvre, who collected some of the data used in this thesis, wrote  
122 several software tools I used to analyze the data and advised me several times throughout  
123 this project.
- 124 Thank you to my labmates at McGill University, Dr. Tony Kwan, Kathrin Brunner, John  
125 McGowan and Charlie Chen. Kathrin taught me mechanical skills that I will apply elsewhere.  
126 Tony, manager of the laboratory, created the most encouraging, trusting and productive work  
127 environment I have ever been apart of.
- 128 Thank you to the friends I can call on at anytime, and thank you to my family whose  
129 constant support makes every step possible.

## Contribution of authors

I, the author, was involved in collecting the cosmic ray data from September 2019 - March 2021. I did not design the cosmic ray testing procedure nor write the data preparation software, but I participated in using the software to analyze cosmic ray results. In the thesis, the terms “clustering,” “local offset” and “relative local offset” are defined. Cosmic ray clustering was done in the data preparation software, but I redid the fit afterwards to explore sensitivity to the fit algorithm. With help from Dr. Lefebvre and Dr. Vachon, I helped design the software that calculated the relative local offsets from cosmic ray data. I wrote that software on my own. I was not involved in the design, data collection, data preparation or analysis of the x-ray data. I also was not involved in creating an alignment model from the x-ray data. I used the x-ray local offsets calculated using x-ray data analysis software to calculate relative local offsets with x-rays. I did the comparison between the x-ray and cosmic ray data.

I hereby declare that I am the sole author of this thesis. This is a true copy of the thesis, including any required final revisions, as accepted by my examiners.

<sup>145</sup>

# Chapter 1

<sup>146</sup>

## Introduction

<sup>147</sup> The Standard Model (SM) is a theoretical framework that describes experimental observa-  
<sup>148</sup> tions of particles and their interactions at the smallest distance scales; however, the questions  
<sup>149</sup> the SM does not address motivate more experimentation.

<sup>150</sup> Accelerators collide particles to generate interactions that can be recorded by detectors  
<sup>151</sup> for further study. Detectors measure the trajectory and energy of all secondary particles  
<sup>152</sup> produced in collisions to understand the interaction. The Large Hadron Collider (LHC) [1]  
<sup>153</sup> at CERN is the world’s most energetic particle accelerator. Its energy makes it a unique  
<sup>154</sup> tool to study elementary particles and their interactions in an environment with conditions  
<sup>155</sup> similar to what would have existed in the early universe. If study at the energy frontier is  
<sup>156</sup> to continue, the LHC must go on.

<sup>157</sup> After 2025, the statistical gain in running the LHC further without significant increase in  
<sup>158</sup> beam intensity will become marginal. The High Luminosity Large Hadron Collider (HL-  
<sup>159</sup> LHC) project [2] is a series of upgrades to LHC infrastructure that will allow the LHC  
<sup>160</sup> to collect approximately ten times more data than in the initial design by  $\sim$ 2030. The  
<sup>161</sup> increase in LHC beam intensity will result in a large increase in collision rate that will make  
<sup>162</sup> accessible and improve statistics on several measurements of interest [3], many only possible  
<sup>163</sup> at the LHC and the energy frontier. The increase in beam intensity will also increase the  
<sup>164</sup> level of background radiation, requiring major upgrades to the experiments used to record  
<sup>165</sup> the outcomes of the particle collisions.

<sup>166</sup> The ATLAS experiment [4] is one of the LHC’s general-purpose particle detector arrays, po-  
<sup>167</sup> sitioned around one of the collision points of the LHC. During the 2019-2022 Long Shutdown  
<sup>168</sup> of the LHC, the most complex upgrade of the ATLAS experiment is the replacement of the  
<sup>169</sup> small wheels of the muon spectrometer with the so-called New Small Wheels (NSWs) [5].

170 The detector upgrade addresses both the expected decrease in hit efficiency of the precision  
171 tracking detectors and the high fake trigger rate expected in the muon spectrometer at the  
172 HL-LHC. The NSWs are made of two different detector technologies: micromegas and small-  
173 strip thin gap chambers (sTGCs). Micromegas are optimized for precision tracking while  
174 sTGCs are optimized for rapid triggering, although each will provide complete coverage and  
175 measurement redundancy over the area of the NSWs. Eight layers each of sTGCs cover the  
176 NSWs. Practically, countries involved in detector constructor created quadruplet modules of  
177 four sTGCs glued together that were arranged and installed over the area of the NSWs once  
178 they arrived at CERN. Teams across three Canadian institutions built and characterized 1/4  
179 of all the required sTGCs.

180 The sTGCs are gas ionization chambers that consist of a thin volume of gas held between two  
181 cathode boards. One board is segmented into strip readout electrodes of 3.2 mm pitch. The  
182 position of the particle track in the precision coordinate can be reconstructed from the strip  
183 signals [5]. The sTGCs achieved the design track spatial resolution in the precision coordinate  
184 of less than 100  $\mu\text{m}$  per detector plane that will allow them to achieve a 1 mrad track angular  
185 resolution using the 8 layers of sTGC on the NSW [6, 5]. The NSW measurement of the  
186 muon track angle will be provided to the ATLAS trigger and used to reject tracks that do  
187 not originate from the interaction point [5].

188 The precise measurement of a muon track angle depends on knowing the position of each  
189 readout strip within the ATLAS coordinate system. To achieve this, the position of specific  
190 locations on the surface of sTGC quadruplets will be monitored by the ATLAS alignment  
191 system to account for time-dependent deformations [5]. Within a quadruplet module, the  
192 strip positions could have been shifted off of nominal by non-conformities of the strip pattern  
193 etched onto each cathode boards [7] and shifts between strip layers while gluing sTGCs into  
194 quadruplets.

195 An x-ray gun was used to measure the offset of strips from their nominal position at the  
196 locations that will be monitored by the ATLAS alignment system thereby providing, locally,  
197 an absolute “as-built” strip position within the ATLAS coordinate system. Estimates of the  
198 “as-built” positions of every readout strip are obtained by building an alignment model from  
199 the available x-ray measurements [8].

200 The technique of measuring the “as-built” strip positions using x-ray data has never been  
201 used before and must be validated. This thesis describes the use of cosmic muon data,  
202 recorded to characterize the performance of each Canadian-made sTGC module, to validate  
203 the x-ray strip position measurements. A description of how this work fits within the overall  
204 alignment scheme of the NSW is also presented.

205 Chapter 2 gives a brief overview of high energy particle physics necessary to understand the  
206 physics motivation of the HL-LHC and NSW upgrades. Chapters 3 and 4 present additional

207 details on the LHC, ATLAS, the NSWs, and sTGCs. In chapter [5](#), the cosmic ray testing  
208 procedure and how the position of the strips can be probed with cosmics data is presented.  
209 Chapter [6](#) introduces the x-ray method, and in chapter [7](#), the x-ray offsets are validated with  
210 cosmic muon data. The thesis concludes with a summary and outlook in chapter [8](#).

211 **Chapter 2**

212 **High energy particle physics**

213 Particle physics aims to study the elementary constituents of matter. Understanding the fundamental building blocks and how they interact provides insight into how the early universe evolved to the forms of matter we observe today. This chapter introduces general concepts in particle physics relevant to understanding the physics goals of the High-Luminosity LHC (HL-LHC) and NSWs upgrade.

218 The information on particle physics and the SM presented here is rather general; the interested reader is referred to [9, 10, 11] for more information.

220 **2.1 The Standard Model**

221 The Standard Model (SM) is a theoretical framework developed in the early 1970's that describes the observed elementary particles and their interactions. It is built on a collection of quantum field theories and has been remarkably successful at predicting experimental observations, including but not limited to the existence of the top quark [12], the tau neutrino [13] and the Higgs boson [14, 15].

226 The known elementary particles described by the SM are represented in figure 2.1. There are 12 matter particles (six quarks and six leptons), 4 force-mediating particles, and the Higgs boson. Each matter particle also has an anti-matter particle pair with the same mass but opposite charge, not represented in figure 2.1. The different forces of nature are understood to be the result of the exchange of force-mediating particles between interacting (coupled) particles. Photons are mediators of the electromagnetic force, W<sup>+</sup>/- and Z bosons are mediators of the weak force, and gluons are mediators of the strong force. At high

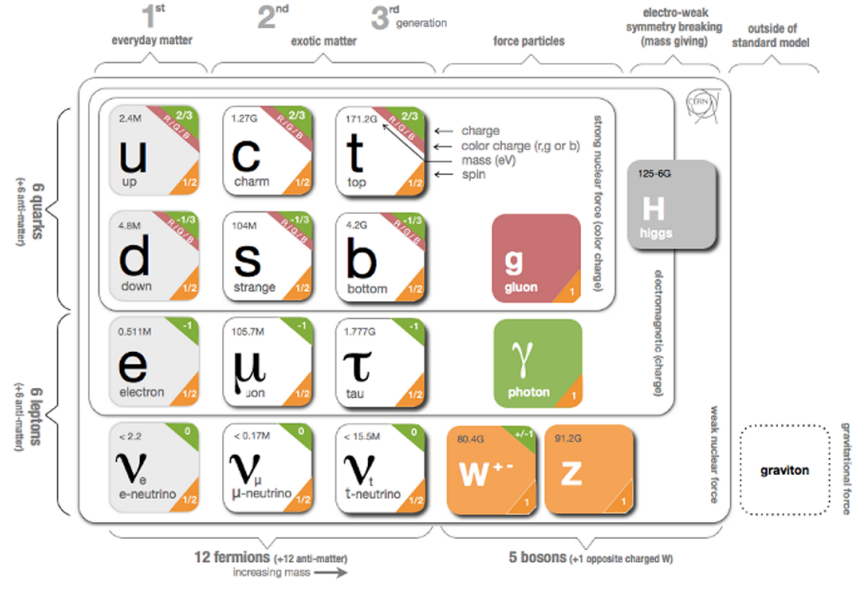


Figure 2.1: Schematic diagram of all elementary particles in the SM. Particles are grouped according to their properties and the forces through which they interact with other particles [16].

233 energy, the SM describes the electromagnetic and weak forces as stemming from a unified  
 234 electroweak force. The Higgs boson field interacts with the particles mediating the unified  
 235 electroweak force to distinguish the weak and electromagnetic forces from each other at lower  
 236 energies and give particles (except neutrinos) a mass. This is called electroweak symmetry  
 237 breaking.

238 Quarks are matter particles that are sensitive to all forces; notably they are the only particles  
 239 sensitive to the strong force. Protons and neutrons are made up of quarks and gluons, and the  
 240 strong force is responsible for their existence and mutual attraction into nuclei [17]. Leptons  
 241 are particles not sensitive to the strong force. Charged leptons include the electron, which  
 242 once part of atoms is responsible for chemistry. Of particular importance for this thesis is  
 243 the charged lepton called a muon. It is like the electron but its mass is  $\sim 200$  times larger  
 244 than that of the electron. Muons have a lifetime of  $2.2 \mu\text{s}$  [11] and decay predominantly as  
 245  $\mu \rightarrow e^- \bar{\nu}_e \nu_\mu$ . Neutrinos are neutral, almost massless leptons that only interact through the  
 246 weak force.

247 Common matter is made up of the lightest constituents of the SM: up and down quarks,  
248 electrons and photons. The other particles are produced in high-energy environments but  
249 then decay to the lightest constituents. Such high energy environments include the condi-  
250 tions present in the early universe [18], astrophysical sources, and particle accelerators. The  
251 presence of the particles of the SM at the beginning of the Universe means that their inter-  
252 actions and decays are fundamental for the study of the evolution of the early universe [18].  
253 Many high energy astrophysical sources, like supernovae, generate particles that rain down  
254 on Earth as cosmic rays [19]. Particle accelerators have been built to create controlled en-  
255 vironments of high-rate, high-energy particle collisions at high energy where the production  
256 and decay of elementary particles can be directly studied.

## 257 2.2 Beyond the Standard Model

258 Despite its success at describing most experimental observations to date, there is ample  
259 evidence that the SM is not a complete description of natural phenomena at the smallest  
260 scales. For example, the SM has a large number of free parameters, the values of which have  
261 to be fine-tuned to fit experimental observations. This is part of the so-called “naturalness”  
262 problem.

263 Furthermore, the SM provides no explanation for several open questions in particle physics.  
264 First, neutrinos in the SM are assumed to be massless and do not gain mass in the same way  
265 as the other particles. However, neutrino were confirmed to change between their different  
266 flavours in 2013 [20], which can only occur if neutrinos do have mass [21]. The neutrino  
267 mass requires physics beyond the standard model [22]. Second, several astrophysical and  
268 cosmological measurements suggest the presence of “dark matter” making up 85 % of the  
269 matter content of the universe [23]. The nature of dark matter is unknown and so far there  
270 is no SM explanation [24]. Third, the SM does not explain the origin and nature of the  
271 matter-antimatter asymmetry that produced our matter-dominated universe. Finally, the  
272 SM does not include a description of gravity.

273 Theoretical extensions beyond the Standard Model (BSM) aim to address some of these  
274 questions, often predicting existence of yet-unseen elementary particles or physics phenomena  
275 beyond those predicted by the SM. These hypothetical new physics phenomena or new  
276 particles can be searched for at particle accelerators.

277 **2.3 Studying high energy particle physics with accelerators**

278

279 In particular, particle accelerators of increasingly higher energy have a long history of enabling the discovery of predicted particles. These include, for example, the discovery of 280 the W [25, 26] and Z bosons [27, 28], the top quark [29, 30], and most recently, the Higgs 281 boson [31, 32]. The discovery of the Higgs boson marked the completion of the SM as it is 282 known today.

284 Based on the established success of the SM, there are two approaches to particle physics 285 research. One approach is to search for the existence of new physics phenomena predicted 286 to exist in BSM theories and the other is to test the validity of the SM to a high degree of 287 accuracy to search for flaws in the model. Standard Model predictions are generally expressed 288 in terms of the probability of a specific physics process to occur, expressed as a cross section 289 in units of barns (with 1 barn =  $10^{-28}$  m<sup>2</sup>). As an example, figure 2.1 shows a summary 290 of cross section measured for different physics processes using the ATLAS experiment and 291 their comparison with the predictions of the SM. Most cross section measurements agree 292 well within one standard deviation with the SM predictions.

293 Particle accelerators provide a controlled and high-collision rate environment that makes 294 them ideal places to search for new physics phenomena and to carry out systematic tests of 295 the SM. The LHC is the highest energy collider in the world so it can access physics that 296 no other accelerator can. A description of the LHC and the ATLAS detector are provided 297 in the next chapter.

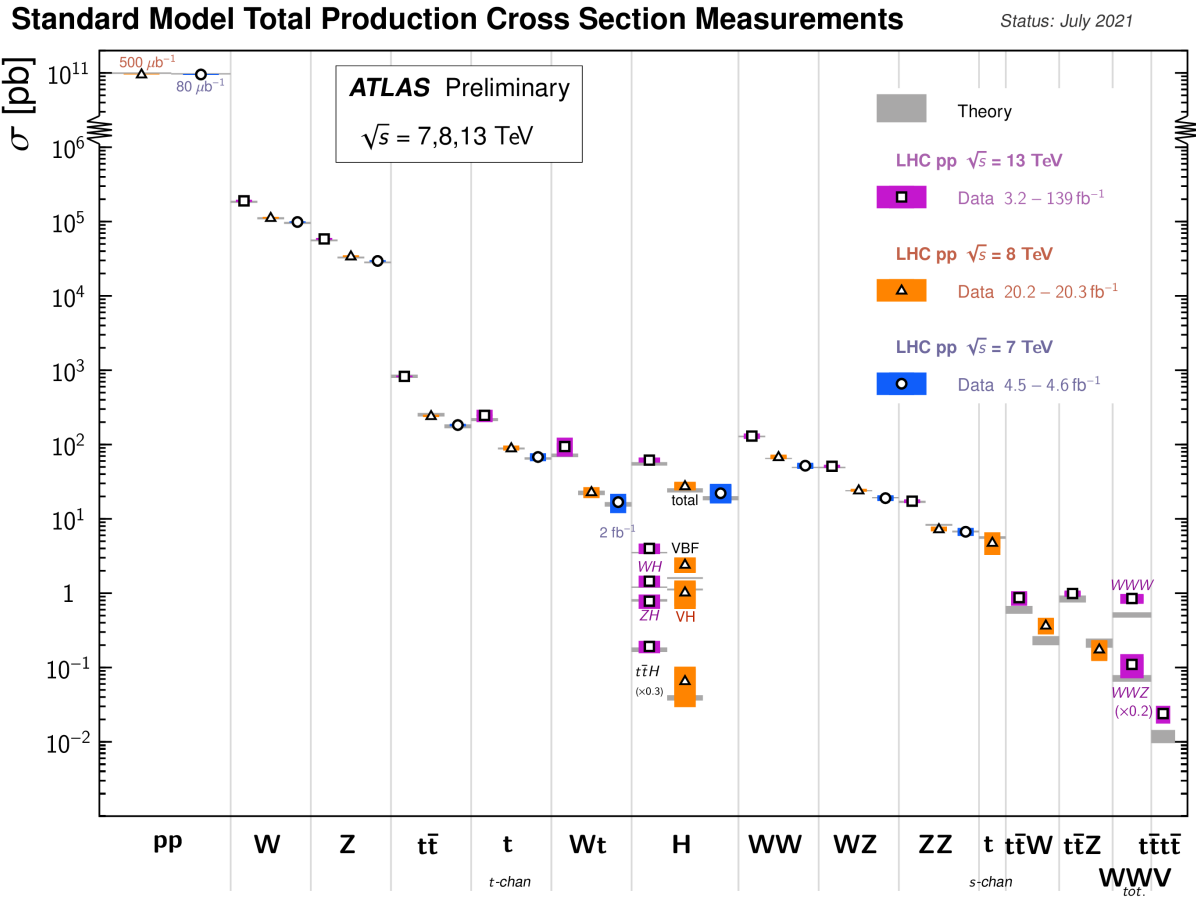


Figure 2.2: Production cross sections of different final states measured by the ATLAS experiment at the LHC. Comparison with the SM theory predictions is also shown [33].

298 **Chapter 3**

299 **The LHC and the ATLAS experiment**

300 The Large Hadron Collider (LHC) is the world’s most energetic particle accelerator and the  
301 ATLAS experiment is used to record the results of particle collisions at the LHC. In this  
302 chapter, details about both that are necessary to understand the High-Luminosity LHC (HL-  
303 LHC) upgrade project and the ATLAS experiment’s New Small Wheels (NSWs) upgrade  
304 are presented.

305 **3.1 The Large Hadron Collider**

306 The LHC is an accelerator 27 km in circumference and located  $\sim$ 100 m underground at  
307 the CERN laboratory near Geneva, Switzerland [1]. It has two beam pipes within which  
308 bunches of protons counter-circulate before being collided in the center of one of four major  
309 experiments, such as the ATLAS experiment (discussed in section 3.3). Protons are guided on  
310 the circular trajectory using 1232 superconducting dipole magnets capable of a maximum  
311 field of 8.33 T. Radio-frequency accelerating cavities are used to accelerate protons to a  
312 the maximum design energy of 7 TeV [34]. During LHC Run-1 (2011-2012), protons were  
313 collided at a collision center-of-mass energy of 7 TeV and 8 TeV [35]. During LHC Run-2  
314 (2015-2018), the center-of-mass energy of proton collisions was increased to 13 TeV [36],  
315 close to the maximum design value of 14 TeV [34]. It is not actually the protons that  
316 interact, but the constituent quarks and gluons that each carry some fraction of the energy  
317 and momentum of the collisions.

318 **Luminosity**

319 The number of proton-proton interactions generated by the LHC directly affects the statistics

available to make measurements of interaction cross sections. Predicting the number of proton-proton interactions requires defining a metric called luminosity [11]. The luminosity of a particle collider is the number of particles an accelerator can send through a given area per unit time. It is calculated from the measurable quantities in Equation 3.1:

$$\mathcal{L} = \frac{f N_1 N_2}{4\pi\sigma_x\sigma_y}, \quad (3.1)$$

where  $f$  is the frequency of the bunch crossings (25 ns),  $N_1$  and  $N_2$  are the number of protons in each bunch ( $\sim 10^{11}$  protons / bunch), and  $\sigma_x$  and  $\sigma_y$  are the RMS of the spatial distributions of the bunch. Therefore, luminosity is a property of accelerator beams, which are set by the capabilities of the accelerator. The design luminosity of the LHC was  $10^{34} \text{ cm}^{-2}\text{s}^{-1}$ . The units of luminosity are an inverse area; multiplying the luminosity by the cross section of a given process gives the expected rate for that process.

Integrating the *instantaneous* luminosity (equation 3.1) over a period of data collection time gives the integrated luminosity,

$$L = \int \mathcal{L}(t) dt \quad (3.2)$$

which is related to the total number of interactions. In this way, the luminosity is the link between the accelerator and the statistical power of measurements to be made with the data collected. So far, the LHC provided an integrated luminosity of  $28.26 \text{ fb}^{-1}$  in Run-1 [35] and  $156 \text{ fb}^{-1}$  in Run-2 [36].

## 3.2 The High-Luminosity LHC

At the end of the LHC program in 2025, the statistical gain on measurements in running the LHC further will become marginal. The HL-LHC [2] project consists of the upgrade of LHC infrastructure to achieve a nearly ten fold increase in instantaneous luminosity, thereby improving measurement statistics as well. Also, some systems will need repair and replacement to operate past  $\sim 2020$ . The LHC will continue to be the most energetic accelerator in the world for years to come and is the only accelerator with enough energy to directly produce the Higgs boson and top quarks. Therefore, the European Strategy for Particle Physics made it a priority “to fully exploit the physics potential of the LHC” with “a major luminosity upgrade” [37]. The goal is for the HL-LHC to provide an integrated luminosity of  $3000 \text{ fb}^{-1}$  in the 12 years following the upgrade. The luminosity actually



Figure 3.1: The LHC/HL-LHC timeline [38]. The integrated luminosities collected and projected for each run of the LHC are shown in blue boxes below the timeline and the center of mass energy of the collisions is shown in red above the timeline. The top blue arrow labels the run number. The acronym “LS” stands for “long shutdown” and indicates periods where the accelerator is not operating. During the shutdowns, upgrades to the LHC and the experiments are taking place. This timeline was last updated in January, 2021, and reflects changes in the schedule due to the ongoing pandemic.

347 achieved will depend on a combination of technological advances and upgrades in progress  
 348 that affect the factors contributing to luminosity defined in equation 3.1 [2]. Figure 3.1 shows  
 349 the projected schedule of the HL-LHC upgrades and operation [38].

350 One of the most anticipated measurements at the HL-LHC is the value of the triple-Higgs  
 351 coupling. Measuring the coupling will allow the determination of the shape of the Higgs  
 352 potential responsible for electroweak symmetry breaking. Any discrepancy with respect to  
 353 the SM prediction will show that there must be other sources of electroweak symmetry  
 354 breaking, and hence physics phenomena beyond the SM. The LHC is the only accelerator  
 355 where the Higgs boson can be produced directly so it is the only place where the triple-Higgs  
 356 coupling could be measured. The HL-LHC upgrade is required to produce a significant  
 357 sample of Higgs produced in pairs to make a statistically meaningful measurement [3, 39].

358 Accordingly, detector sensitivity to various Higgs decays will be important at the HL-LHC.

### 359 3.3 The ATLAS experiment

360 The ATLAS experiment [4] was designed to support all the physics goals of the LHC. It  
361 is 44 m long and 25 m in diameter, and weighs 7000 tonnes. The ATLAS experiment is  
362 centered around one of the LHC's interaction points (a place where the beams collide). As  
363 shown schematically in figure 3.2, ATLAS consists of an array of particle detector subsystems  
364 arranged concentrically around the beam pipe. The ATLAS experiment is cylindrical because  
365 it aims to provide  $4\pi$  coverage around the interaction point. In reference to the cylindrical  
366 geometry of the experiment, it is helpful to separate the subsystems of ATLAS into the  
367 so-called "barrel" and "endcap"/"forward" regions.

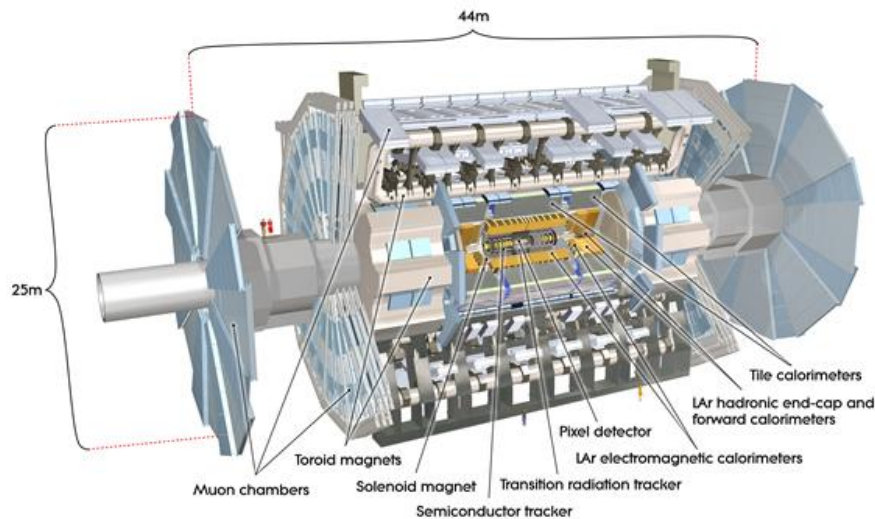


Figure 3.2: Schematic diagram of the ATLAS experiment, with the various detector subsystems labelled [4].

368 For analysis purposes, a spherical coordinate system is defined. The azimuthal angle  $\phi$  is  
369 measured around the beampipe and the polar angle  $\theta$  is measured from the beam pipe. The  
370 polar angle is more often expressed in terms of pseudo-rapidity, defined as  $\eta = -\ln \tan(\theta/2)$ .  
371 Pseudo-rapidity values vary from 0 (perpendicular to the beam) to  $\pm\infty$  (parallel to the  
372 beam, defined as the z-direction) and is an approximation to the rapidity of a particle when  
373 its momentum is much greater than its mass. It is useful to describe the direction of outgoing

374 particles in proton-proton collisions because differences in rapidity are invariant to a Lorentz  
375 boost along the beam direction.

376 The ATLAS experiment provides identification and kinematic measurements for each particle  
377 created after the initial collision, which is done by assembling offline the information recorded  
378 by each subsystem. With this information, signatures of processes of interest can be identified  
379 and studied. An overview of the main ATLAS subsystems is given below.

### 380 **The inner detector**

381 The inner detector [40, 41] (figure 3.3) is for precise measurements of charged particle tra-  
382 jectories, measurement of primary and secondary interaction vertices and assistance in the  
383 identification of electrons. A 2 T solenoid with field parallel to the beam bends the trajec-  
384 tory of outgoing charged particles. A measurement of the bending radius of each charged  
385 particle provides information about its momentum. The innermost part of the inner tracker  
386 is made of high-resolution semiconductor pixel and strip detectors while the outermost part  
387 is made of straw-tubes. The straw tubes are used in the trajectory measurements but they  
388 are also interspersed with material designed to enhance the creation of transition radiation.  
389 Transition radiation occurs when a highly relativistic charged particle traverses a material  
390 boundary [42]. The amount of transition radiation emitted by a charged particle is detected  
391 by the straw-tubes and is used to identify electrons.

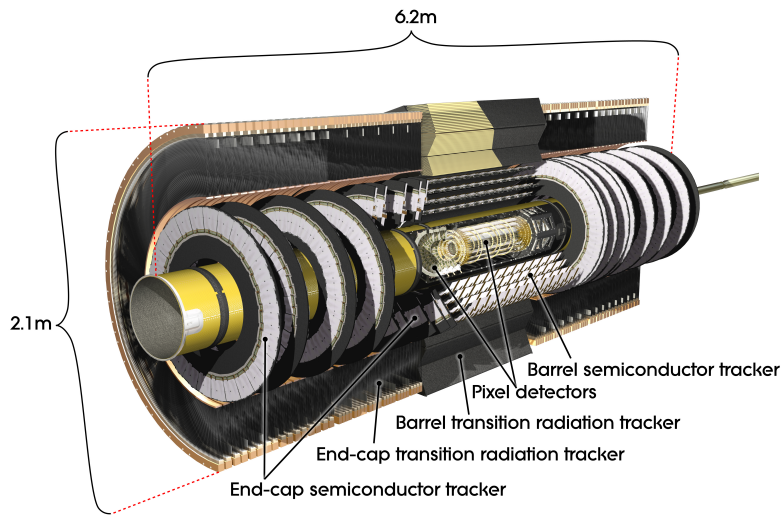


Figure 3.3: Schematic diagram of the ATLAS experiment's inner detector, with the different segments and the technology used labeled [4].

392 **Calorimetry system**

393 Electromagnetic and hadronic sampling calorimeter units are used to record the energy  
394 of electrons, photons and jets<sup>1</sup>. A combination of liquid-argon (LAr) electromagnetic and  
395 hadronic calorimeters [43] and tile-scintillator hadronic calorimeters [44] cover the rapidity  
396 range  $|\eta| < 4.9$ , as shown in figure 3.4.

397 Sampling calorimeters have alternating layers of dense material and material that can mea-  
398 sure the amount of ionization by charged particles. The dense material causes incoming  
399 charged particles to shower into lower energy particles and deposit their energy in the sen-  
400 sitive volume. Only muons and neutrinos are known to pass the calorimeters to the muon  
401 spectrometer without being absorbed.

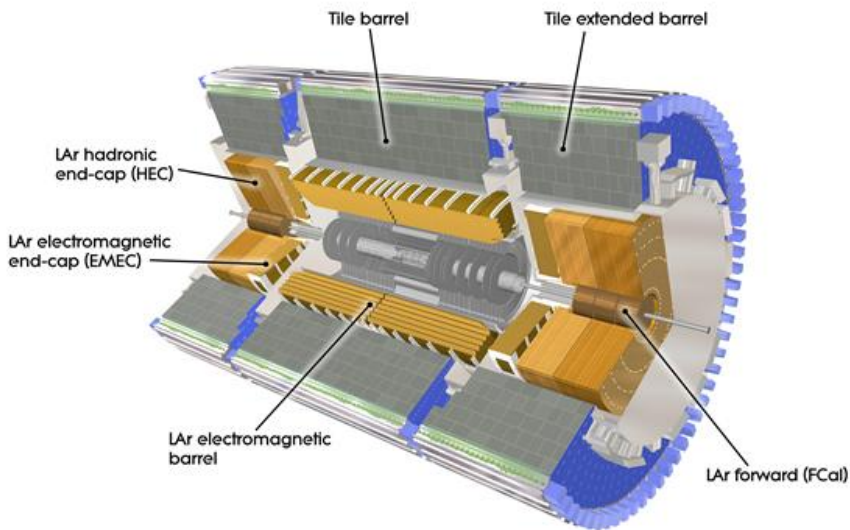


Figure 3.4: Schematic diagram of the ATLAS calorimeter system, with the different segments and the technology used labeled [4].

402 **Muon spectrometer**

403 The muon spectrometer [45] consists of multiple layers of tracking chambers embedded in  
404 a 2 T magnetic field generated by an air-core superconducting toroid magnet system. Fig-  
405 ure 3.5a shows a schematic diagram of the layout of the different chambers and of the toroid

<sup>1</sup>When quarks or gluons are expelled in a high energy collision, they create collimated groups of hadrons called jets because they carry a charge called “colour”, and nature only allows “colourless” combinations to exist [42].

406 magnets [4]. The trajectory of a muon is reconstructed from the information recorded by  
 407 the different types and layers of tracking chambers. The amount of bending in the magnetic  
 408 field provides a measure of the muon's momentum. In the barrel section of ATLAS, the  
 409 toroidal magnetic field is created by eight coils bent into the shape of a "race-track" and  
 410 symmetrically arranged around the beampipe. In the forward region, two end-cap toroids,  
 411 each with eight smaller racetrack-shaped coils arranged symmetrically around the beam pipe  
 412 are inserted in the ends of the barrel toroid [46].

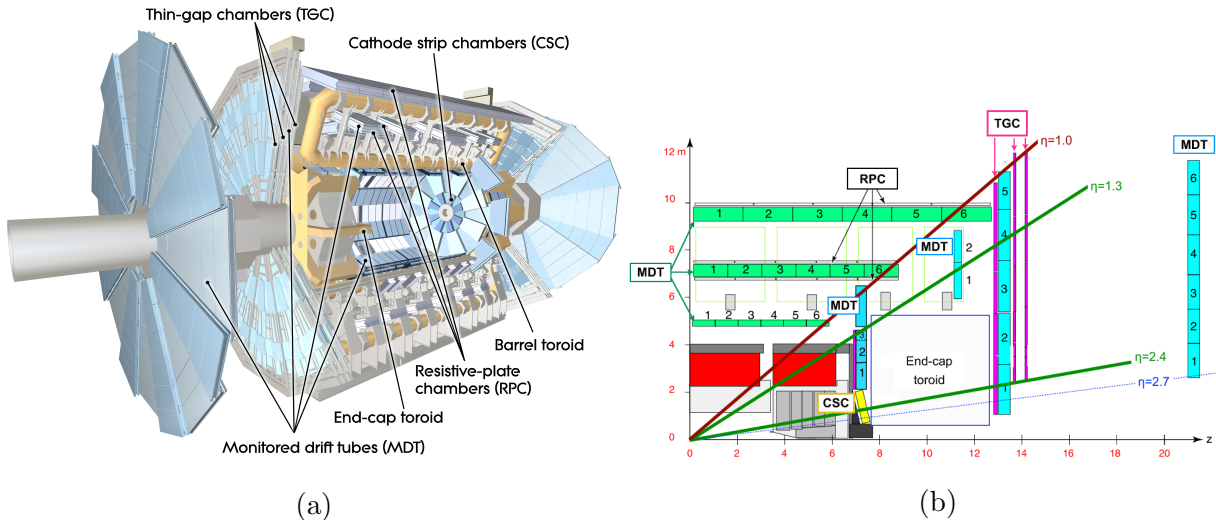


Figure 3.5: Schematic diagram of the ATLAS muon spectrometer. Figure (a) shows a 3D projection of the system with the different types of chambers and different parts of the toroidal magnet system labeled [4]. Figure (b) shows a projection of one quarter of the muon spectrometer, with the interaction point in the bottom left corner. The small wheel is just left of the end cap toroid, the big wheel is to its right, and the outer wheel is the rightmost structure [47].

413 The muon spectrometer is separated into detectors used for precision offline tracking and  
 414 for triggering purposes. Three layers of monitored drift tubes (MDTs) or cathode strip  
 415 chambers (CSCs) are used for tracking. The position of the muon track in each of the three  
 416 layers allows reconstruction of the bent trajectory of a muon and hence its momentum. To  
 417 satisfy the muon spectrometer target momentum resolution of  $\Delta p_T/p_T < 1 \times 10^{-4} p / \text{GeV}$   
 418 for  $p_T < 300 \text{ GeV}$  and a few percent for lower  $p_T$  muons, the MDTs and CSCs were designed  
 419 to achieve a spatial resolution of  $50 \mu\text{m}$  each. Accordingly, an optical alignment system was  
 420 designed to monitor and correct for chamber positions [45, 48].

421 Resistive plate chambers (RPCs) are used for triggering in the barrel and thin-gap chambers

422 (TGCs) are used for triggering in the endcaps. The positions of each type of chamber  
423 are sketched in figure 3.5b. The endcap section of the muon spectrometer consists of three  
424 sections, the small wheel, big wheel, and outer wheel – ordered by proximity to the interaction  
425 point. In Run-1, low (high)  $p_T$  muons were triggered on if two (three) of the RPC or TGC  
426 layers around the big wheel fired in coincidence, for the barrel and endcaps respectively [49].  
427 After Run-1 it was discovered that up to 90% of the triggers in the endcap were fake, caused  
428 by background particles generated in the material between the small wheel and the big  
429 wheel [5]. To reduce the fake rate in Run-2, the TGCs on the inside of the small wheel also  
430 had to register a hit. The added condition reduced the trigger rate by 50% in the range  $1.3 < |\eta| < 1.9$  [50]. The effectiveness of the solution was limited since the  $|\eta|$ -range of the small  
432 wheel TGCs was limited to  $1.0 < |\eta| < 1.9$  and the spatial resolution of the small wheel  
433 TGCs is coarse [5].

434 **Trigger system**

435 It would be impossible to record all the data from bunch crossings every 25 ns, corresponding  
436 to a rate of  $\sim 40$  MHz. The ATLAS experiment has a multi-level trigger system to select  
437 events of interest for permanent storage. The Level-1 (L1) hardware trigger [49] uses partial-  
438 granularity information from the muon spectrometer and calorimeters to trigger on high  $p_T$   
439 muons, electrons, jets, missing transverse energy, and  $\tau$  decaying to hadrons. After Run-3  
440 an upgrade of the trigger system will allow a maximum trigger rate of 1 MHz with a latency  
441 of 10  $\mu$ s [51], but for now the working limits are a rate of 100 kHz [50] and 2.5  $\mu$ s [49].

442 The L1 trigger is used to define regions of interest that are fed into the software high level  
443 trigger (HLT) [52], in which the full granularity of the muon spectrometer and calorimeter  
444 are used with information from the inner detector to reduce the trigger rate to 1 kHz. Events  
445 that satisfy at least one of the L1 and HLT trigger criteria are recorded to permanent storage  
446 for offline analysis.

447

---

448 With the foreseen increase in luminosity at HL-LHC, it is a priority to upgrade the ATLAS  
449 detector to further reduce the muon trigger fake rate in the forward region. The New Small  
450 Wheels being commissioned to replace the original ATLAS muon small wheels will address  
451 this challenge.

452 **Chapter 4**

453 **The New Small Wheels**

454 **4.1 Motivation for the New Small Wheels**

455 The hit rate of all detector systems will significantly increase during HL-LHC operation  
456 because of the increase in luminosity. The increased rate presents a challenge for both the  
457 tracking and triggering capabilities of the muon spectrometer [5].

458 In terms of precision tracking, the maximum hit rate in the MDTs is expected to reach above  
459 300 kHz by the end LHC operation. At this rate, the hit efficiency of MDTs decreases by  
460 35%, mostly due to the long dead-time of the chambers. Losing hits in the small wheel will  
461 reduce the high  $p_T$  muon momentum resolution. The decrease in resolution will affect the  
462 ability to search for, for example, the decay of hypothetical heavy bosons ( $W'$ ,  $Z'$ ) or other  
463 hypothetical particles beyond the SM [3].

464 Already during LHC Run-2 operation, the forward muon trigger system had to cope with a  
465 very high fake rate, even with the inclusion of TGC data from the small wheel as part of the  
466 trigger criteria. At the luminosity expected in Run-3, it is estimated that 60 kHz out of the  
467 maximum L1 trigger bandwidth of 100 kHz would be taken up by forward muon triggers.  
468 To address this challenge, a possible solution would be to raise the minimum  $p_T$  threshold  
469 from 20 GeV to 40 GeV. However, this would have an adverse impact on the ability to study  
470 several physics processes of interest that depend on low  $p_T$  muons, particularly the Higgs  
471 decay to two muons, the Higgs decay to two tau leptons and hypothetical particle decays  
472 beyond the SM [5].

473 The NSWs will address both of these problems. They will be made of precision tracking  
474 chambers suitable for the expected hit rates during the HL-LHC and triggering chambers  
475 capable of 1 mrad track angular resolution. The idea behind the design triggering capability



Figure 4.1: A schematic diagram of a quarter cross section of the ATLAS muon spectrometer, with the interaction point (IP) in the bottom left corner. Three possible tracks are labeled. Ideally, track A would be triggered on while track B and C discarded. With the old small wheel, all three tracks would be recorded. With the NSW, only track A would be recorded [5].

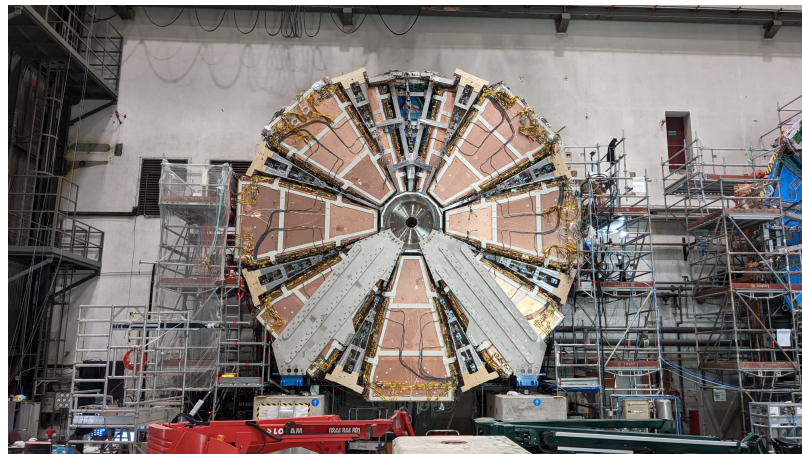
476 of the chambers is to allow matching of track segments measured by the NSW with track  
 477 segments from the big wheel to discard tracks not originating from the interaction point.  
 478 Figure 4.1 illustrates this point: the Run-2 trigger system would have triggered on all three  
 479 tracks (A, B, C) while with the NSW the trigger system would only trigger on track A.  
 480 The NSWs will therefore make it possible to maintain a low muon  $p_T$  trigger threshold and  
 481 maintain an adequate muon momentum resolution during HL-LHC operations, which will  
 482 allow the full exploitation of the physics potential of this research program [5].



(a) A sTGC quadruplet module. The left image highlights the trapezoidal shape of a quadruplet module. The right image shows the corner at the short edge, where the four sTGC layers and each layer's gas inlet are visible. The gas outlets and high voltage cables are located along the long edge near the corner in the back left of the photo. The green printed circuit board along the sides are the adaptor boards where the front end electronics are attached.



(b) Left: A sTGC wedge. The white frame outlines the individual quadruplet modules that have been glued together into a wedge. Right: A completed sector, with two sTGC wedges on the outside and two micromegas wedges on the inside.



(c) A picture of one of the two NSWs. All sectors except one large sector at the top are installed, revealing two of the smaller sectors that are normally hidden under the large sectors and support bars. The NSWs are 9.3 m in diameter.

Figure 4.2: Images showing different stages of NSW construction.

483 **4.2 Design of the NSWs**

484 The NSWs are made with two detector technologies: micromegas and small-strip thin gap  
485 chambers. Eight layers of each cover the entire area of the wheel. Micromegas are designed  
486 to be the primary precision tracking detectors and sTGCs the primary triggering detectors,  
487 but both technologies offer full redundancy by being capable of providing both precision  
488 measurements and trigger information. Both types of detectors were designed to achieve  
489 spatial resolution better than  $\sim 100 \mu\text{m}$  per layer. Four chambers are glued together to create  
490 quadruplet modules of each detector type. Quadruplets of different sizes, most shaped as  
491 trapezoids, are assembled into wedges. Two sTGC wedges and two micromegas wedges are  
492 layered to create sectors (with the sTGC wedges on the outside) [5]. Different stages of the  
493 construction process are shown in figure 4.2. At the time of writing, the assembly of the  
494 NSWs has just been completed. The first NSW has been lowered into the ATLAS cavern  
495 and is being commissioned and the second will be lowered shortly.

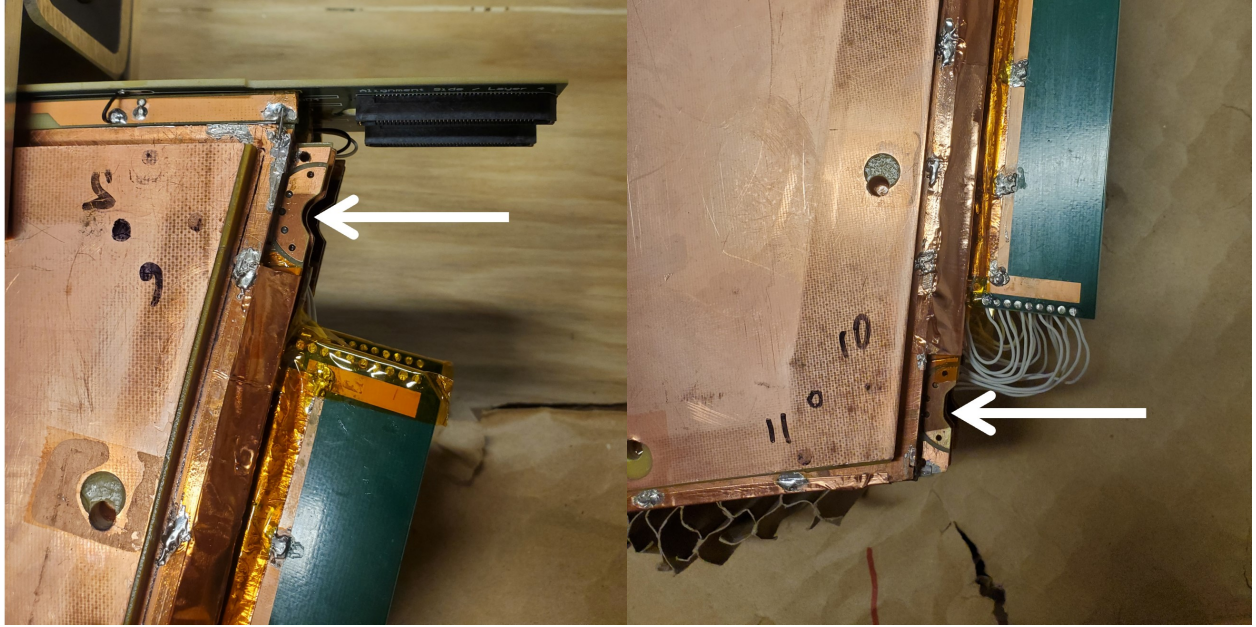
496 **4.3 Small-strip thin gap chambers**

497 The sTGCs are gas ionization chambers operated with a gas mixture of CO<sub>2</sub>:n-pentane with  
498 a ratio of 55%:45% by volume. Gold-plated tungsten wires, 50  $\mu\text{m}$  in diameter and with  
499 1.8 mm pitch, are suspended between two cathode planes made of FR-4, each 1.4 mm away  
500 (see figure 4.3). One cathode board is segmented into copper pads of varying area (with a  
501 typical size of  $\sim 300 \text{ cm}^2$  each), and the other is segmented into copper strips of 3.2 mm pitch  
502 running lengthwise perpendicular to the wires. High voltage is applied to the wires and the  
503 cathode planes are grounded [5, 53]. When a muon passes through a sTGC, it will ionize some  
504 of the atoms in the gas and the electric field in the gas gap will result in the formation of an  
505 ionization avalanche [54]. The motion of the ions and free electrons generates small currents  
506 on the nearby wire and capacitatively-coupled strip and pad electrodes [5]. The gas mixture  
507 was chosen to absorb excess photons produced in the avalanche that delocalize the avalanche  
508 signal [55] and saturate many strip electrodes, preventing the formation of streamers [42].  
509 This allows the chambers to be run at a higher high-voltage providing a faster response and  
510 higher signal [55]. The resistivity of the carbon coating and capacitance of the pre-preg  
511 sheet tune the spread of the charge distribution [56] and the speed of the response [57] to  
512 optimize the rate capability. The combined information from the strip readout electrodes  
513 and wires provide the location where the muon passed through the chamber. The small pitch  
514 of the strip readout electrodes is what allows the quadruplets to deliver good track angular  
515 resolution to improve the fake trigger rate and meet the precision tracking requirements [5].



Figure 4.3: Internal structure of an sTGC, zoomed into the area under a pad. High voltage is applied to wires suspended in the gas volume to create an electric field. A passing muon causes an ionization avalanche that is picked up by the wire, strip and pad electrodes [8].

- 516    A 3-out-of-4 coincidence in pad electrodes from each layer of a quadruplet defines a region of  
 517    interest where the strip and wire electrodes should be read out. The pad triggering scheme  
 518    greatly reduces the number of electrodes that require readout so that a track segment of the  
 519    required angular resolution can be provided quickly enough to the hardware trigger [5].
- 520    Signal is read out from groups of successive wires, so the position resolution in the direction  
 521    perpendicular to the wires is 10 mm per plane. The wires give the azimuthal coordinate  
 522    in ATLAS so the position resolution in this direction is sufficient. Good resolution on the  
 523     $\eta$  coordinate, perpendicular to the strips, is important [5]. In a test beam environment,  
 524    the strip spatial resolution of a single sTGC was measured to be 45 microns for muon  
 525    perpendicularly incident on the surface of the sTGC. Although the spatial resolution worsens  
 526    as function of muon angle measured from normal incidence [58], when four sTGCs are glued  
 527    together into a quadruplet the design angular resolution of 1 mrad in the strip coordinate is



(a) Brass insert near long edge.

(b) Brass insert near short edge.

Figure 4.4: The brass inserts sticking out from the gas volumes of an sTGC quadruplet. These inserts were pressed against alignment pins when the individual sTGCs were being glued together.

528 achievable [5, 53].  
 529 To achieve the required track angular resolution once installed in ATLAS, the absolute  
 530 position of each sTGC strip within the ATLAS coordinate system must be accurately known.  
 531 The degree of accuracy required is on the order of the position resolution of the chambers,  
 532  $\sim 100 \mu\text{m}$ . The NSW alignment system, detailed in section 4.5, will monitor the position of  
 533 alignment platforms installed on the surface of the wedges. The alignment platforms are  
 534 installed with respect to an external reference on the sTGCs: two brass inserts on each strip  
 535 layer on one of the angled sides of each quadruplet (shown in figure 4.4). So the challenge  
 536 of monitoring the position of the strips in ATLAS was separated into two steps: first, infer  
 537 the position of the strips with respect to the brass inserts using the sTGC design geometry;  
 538 second, use the alignment system to monitor the position of the alignment platforms. The  
 539 next section provides some pertinent details on the sTGC construction process, with steps  
 540 that affect the position of the strips with respect to the brass inserts highlighted.

## 541 4.4 sTGC Quadruplet Construction

542 Five countries were responsible for producing sTGC quadruplets of varying geometries for the  
543 NSW: Canada, Chile, China, Israel and Russia. Canada was responsible for the construction  
544 of one quarter of the required sTGCs, of three different quadruplet geometries. The steps of  
545 the construction process in each country were similar [5]. The process followed in Canada is  
546 detailed here.

547 A research group at TRIUMF in Vancouver, British Columbia was responsible for preparing  
548 the cathode boards. The boards were made and the electrodes etched on at a commercial  
549 laboratory, Triangle Labs, in Carson City, Nevada. Once completed they were sent to TRI-  
550 UMF to be sprayed with graphite and to have support structures glued on [7]. The boards  
551 are commercial multilayer printed circuit boards, but the strip boards required precision ma-  
552 chining to etch the strip pattern [5]. Triangle Labs also machined the two brass inserts into  
553 each strip board. A coordinate measuring machine (CMM) was used to accurately measure  
554 the position of a set of reference strips on each board. Four quality parameters describing  
555 non-conformities in the strip pattern of each board with respect to the brass inserts were  
556 derived from the data and the results are available on a QA/QC database. The parameters –  
557 offset, angle, scale and nonparallelism – and the CMM data collection is described in full  
558 in [7]. Due to time constraints, tolerances on the non-conformities in the etched strip pattern  
559 with respect to the brass inserts were loosened, with the condition that the strip positions  
560 in ATLAS would have to be corrected for [7].

561 The prepared boards were sent to Carleton University in Ottawa, Ontario for construction  
562 into sTGCs and quadruplets. First, the wires were wound around the pad cathode boards  
563 using a rotating table and the wires were soldered into place. A wound pad cathode board  
564 was held by vacuum on a granite table, flat to within 20  $\mu\text{m}$ , and a strip cathode board glued  
565 on top to create an sTGC. Holding one sTGC flat with the vacuum, another was glued on  
566 top to create a doublet, then two doublets were glued together to create a quadruplet. When  
567 gluing sTGCs together, the brass inserts were pushed against alignment pins with the goal of  
568 keeping the strip layers aligned within tolerance. However, non-conformities in the shape of  
569 the brass inserts, non-conformities in the position of the alignment pins and shifts between  
570 sTGCs while the glue cured resulted in misalignments between the brass inserts and strip  
571 layers. Precise alignment of the pad boards or wires with respect to the strip boards did  
572 not have to be so tightly controlled because pads and wires do not measure the precision  
573 coordinate.

574 The Carleton team finished the quadruplets by installing adaptor boards on the angled sides  
575 of each layer that allow front end electronics to be attached. Completed quadruplets were  
576 sent to McGill University where their performance was characterized with cosmic rays. De-

577 tails pertaining to cosmic ray testing of sTGC quadruplets at McGill University are described  
578 in chapter 5. Tested quadruplets were sent to CERN where they were assembled into wedges  
579 and alignment platforms installed. The alignment platforms were installed using a jig posi-  
580 tioned with respect to the brass inserts. Completed wedges were assembled into sectors then  
581 installed on the NSWs.

582 The quadruplet construction process had two steps where strip positions could be shifted off  
583 of nominal. At board-level, there could be non-conformities in the etched strip pattern with  
584 respect to the brass inserts, described by the four quality parameters [7]. At the quadruplet  
585 level, misalignments between the brass inserts and strips on different layers were possibly  
586 introduced during the gluing. The result was that the brass inserts were not a reliable  
587 reference point and that the strips can be offset from their design position by up to hundreds  
588 of micrometers. Offsets in strip positions from nominal in Canadian quadruplets were shown  
589 to be random [7], so no one correction would suffice. The offsets must be measured and  
590 corrected for in the ATLAS offline software that does the precision tracking. Understanding  
591 the work ongoing to make measurements of strip position offsets and correct for them requires  
592 understanding the strategy of the NSW alignment system.

## 593 4.5 NSW alignment

594 The idea of the NSW alignment system is presented in [5], but the details have only been  
595 presented internally so far. After the wedges are constructed, alignment platforms are in-  
596 stalled on every sTGC quadruplet and optical fibres routed to them, as shown in figure 4.5.  
597 Light from the optical fibres will be monitored in real time by cameras (BCAMs) mounted on  
598 the alignment bars of the NSWs. The system will thus record the positions of the alignment  
599 platforms in the ATLAS coordinate system and any changes over time.

600 The original alignment scheme was to use the brass inserts as a reference between the align-  
601 ment platforms and the individual strips, as shown in the solid arrows in figure 4.6 – this  
602 will no longer work. The position of the alignment platforms will be known thanks to the  
603 alignment system, so a different method to get the position of the strips with respect to the  
604 alignment platforms is currently in its final stage of development. The technique consists of  
605 the measurement of the strip pattern offset at a few areas on the surface of a sTGC quadru-  
606 plet using an xray gun mounted on the alignment platforms. The local strip pattern offset  
607 with respect to nominal geometry at the location of each alignment platform is obtained  
608 by analyzing the xray gun beam profile. As shown in figure 4.6, this approach essentially  
609 bypasses the need to know the position of strips with respect to the brass inserts. The align-  
610 ment platforms provide the link to the nominal geometry because the nominal group of strips

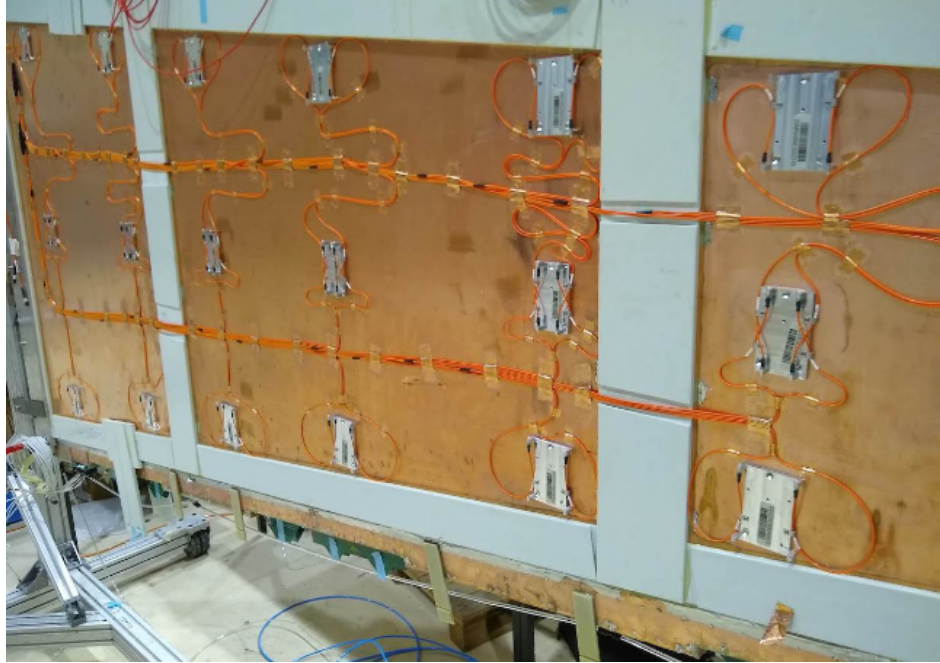


Figure 4.5: A sTGC wedge with alignment platforms (silver) installed on the quadruplet. Optical fibres (orange) are routed to the alignment platforms. Cameras on the frames of the NSWs will record light from the optical fibres to monitor in real-time the position the alignment platforms in the ATLAS coordinate system.

611 that should be nearest to them can be identified using the nominal geometry parameters that  
 612 assume the strips are perfectly etched and aligned. Cosmic muon track positions cannot be  
 613 compared to the nominal geometry because the alignment platforms are not installed when  
 614 cosmics data is collected, so there is no external reference to provide a link to the nominal  
 615 geometry.

616 The x-ray method does not have the sensitivity to measure the offset of each strip from  
 617 nominal, but what can be measured instead is the offset of the strip pattern in a local area  
 618 around the position of the gun. *Local offsets* are used to build an alignment model for each  
 619 strip layer. Formally defined, an alignment model is a set of parameters used to estimate the  
 620 “as-built” position of a strip given its nominal position. The alignment model currently being  
 621 worked on takes x-ray and CMM data as input to calculate an overall offset and rotation of  
 622 each strip layer with respect to nominal [8]. The alignment parameters could be described  
 623 as “global”, meaning over the whole layer instead of local. Without the x-ray dataset, there  
 624 would be no input to the alignment model that takes into account inter-layer misalignments  
 625 introduced during quadruplet construction.

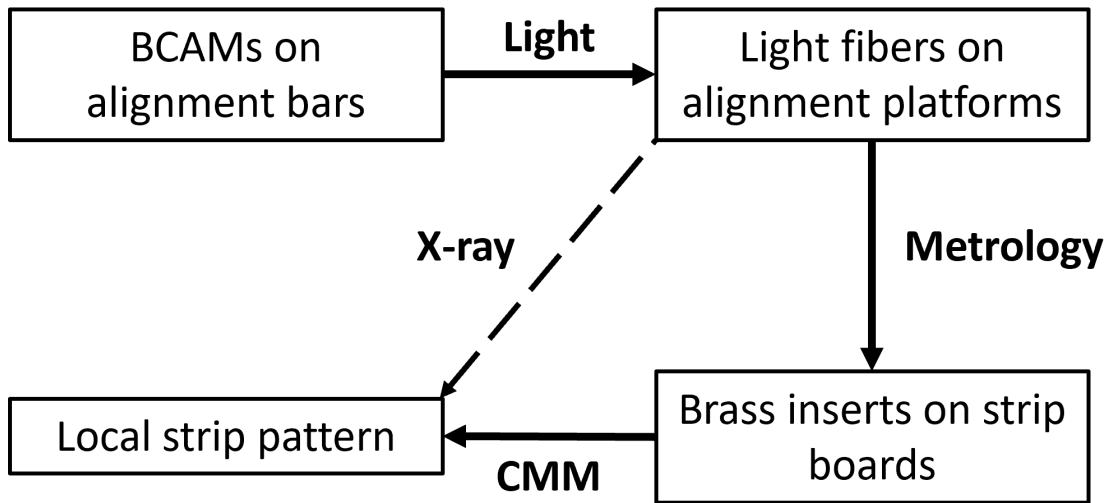


Figure 4.6: Schematic diagram showing how the different elements of the sTGC alignment system relate to one another. The solid arrows denote the planned alignment scheme. The dashed arrow shows the modification being finalized now. This figure was originally designed by Dr. Benoit Lefebvre.

Given that the x-ray local offsets can only be measured at positions where the gun can be attached and that they are an important part of the alignment scheme, the new x-ray measurement technique needs to be validated. The goal of this thesis is to validate the x-ray local offsets while exploring how cosmics data complements and adds to the understanding of strip positions and global alignment.

631 **Chapter 5**

632 **Using cosmic muons to measure  
633 relative strip position offsets**

634 At McGill University, among other quality and functionality tests, each Canadian-made  
635 quadruplet was characterized with cosmic muons. In this chapter, the experimental setup and  
636 how the data was analyzed to provide relative strip position offsets is presented. The analysis  
637 method was motivated by the how the measurements could be compared to measurements  
638 done with the x-ray method (chapter 6) but also it stands alone as a characterization of the  
639 alignment between strips of different layers. The chapter begins with a brief introduction to  
640 cosmic rays.

641 **5.1 Cosmic rays**

642 The earth is being constantly bombarded by particles from the sun, galactic sources and  
643 extra galactic sources – collectively called cosmic rays [19, 11]. Cosmic rays consist mostly  
644 of protons, but also heavier ions, gamma rays and the term sometimes includes neutrinos.  
645 The primary (initial) cosmic ray interacting with the atmosphere causes electromagnetic and  
646 hadronic showers of secondary particles. Hadronic showers result from the primary cosmic ray  
647 interacting strongly with the target of the atmosphere, resulting in an abundant production  
648 of pions. Charged pions predominantly decay to muons (there is a lesser contribution to  
649 the muon flux from kaons as well) [59]. The secondary muons are relativistic and thanks  
650 to time dilation their lifetime is extended as measured in the reference frame of earth, so a  
651 flux of approximately 1 muon/cm<sup>2</sup>/ min reaches the ground [11]. Measuring the muon flux  
652 and energy spectrum reveals information about primary cosmic rays [59] which is interesting

653 to high energy physicists and astrophysicists. The muon flux is also terribly convenient for  
654 testing muon detectors.

655 **5.2 Experimental setup**



Figure 5.1: Cosmic muon hodoscope at McGill University with a sTGC quadruplet module in the test bench.

656 Cosmic muon characterization of sTGC quadruplet modules was done with a hodoscope, a  
657 complete description of which can be found in [58]. The quadruplet was placed in the center  
658 of the test bench. Above and below it was a layer of scintillator-PMT arrays, as shown in  
659 figure 5.1. When a cosmic muon passed within the acceptance of the hodoscope, at least one  
660 scintillator from the top array and at least one from the bottom array fired in coincidence.  
661 A trigger signal was formed using NIM modules from the coincidence of signals from the top

662 and bottom arrays of scintillators. The trigger signal was passed to the front-end electronics  
663 attached to the adaptor boards of each layer of the quadruplet.

664 Operating the chambers also required gas and high voltage. A gas mixture of pentane-CO<sub>2</sub>  
665 in the appropriate proportions was prepared and delivered to each sTGC with a gas system  
666 designed and made at McGill University [60]. Since pentane is flammable, the gas system  
667 was designed with safety top of mind. The gas system was controlled by a slow control  
668 program, also custom made [60]. To prepare the quadruplets for operation, CO<sub>2</sub> was flushed  
669 through them overnight to remove potential impurities within each chamber's gas volume.  
670 Then, the equivalent of approximately five sTGC gas volumes of the pentane-CO<sub>2</sub> mixture  
671 was flushed through to ensure a uniform gas mixture inside the sTGCs; the procedure takes  
672 approximately four hours. High voltage was provided by commercial CAEN high voltage  
673 boards [60].

## 674 5.3 Data acquisition

675 Each sTGC electrode was connected to a channel on a prototype ASIC<sup>1</sup> on the front-end elec-  
676 tronics, attached to the adaptor boards on each layer of a quadruplet. Each ASIC features  
677 64 charge amplifiers with selectable gain and input signal polarities, which output the digi-  
678 tized amplitude of the signal at peak for channels above a pre-defined threshold. Thresholds  
679 were estimated [62] by optimizing the efficiency of detecting muons while minimizing noise,  
680 and further manually tuned in the configuration/readout software before the start of data  
681 acquisition for each quadruplet. The signal from the capacitively-coupled strip electrodes  
682 has positive polarity and is read out with a gain of one. For each trigger, the signal peak  
683 amplitude of all channels above threshold was recorded as an event and stored in a binary  
684 file. The readout of strips made use of a special feature of the custom ASIC, the so-called  
685 “neighbour triggering” function where signals on channels adjacent to those above threshold  
686 are also read out.

687 The quadruplets were held at 3.1 kV for approximately two hours to collect data from  
688 approximately 1 million muon triggers.

---

<sup>1</sup>A custom Application Specific Integrated Circuit (ASIC) named VMM3 [61], designed for the readout of signals from the micromegas and sTGCs of the NSWs.

689 **5.4 Data preparation**

690 **5.4.1 Data quality cuts on electrode hits**

691 Corrupted data, if any, is removed while the raw data is being recorded in a binary file. After  
692 data taking is completed, the raw data is decoded and the electronics channels are mapped  
693 to physical readout electrodes of the quadruplet. The result of this data preparation step is  
694 stored in a ROOT [63] tree data format.

695 A hit is defined as a signal recorded from a channel that was above threshold or (in the  
696 case of strips) neighbour triggered. In addition to hits from muons, the quadruplets record  
697 noise from the electronics and  $\delta$ -rays (electrons liberated with sufficient energy to escape  
698 a significant distance away from the primary radiation and produce further ionization).  
699 Therefore, selection cuts are applied to reduce the number of hits that do not originate from  
700 muons. Readout strips located at the very edge of the cathode board tend to have higher  
701 electronic noise. As a result, all strip hits on a layer where a hit is present on the strips  
702 at either edge of the quadruplet are removed from the analysis. A default pedestal value  
703 is subtracted from the recorded signal peak amplitude of each electrode for a more realistic  
704 estimate of the signal amplitude. Also, events that only have hits on pad electrodes (no  
705 strips or wires) were removed from the analysis since these hits are likely from electronic  
706 noise, which is higher on the pad readout channels due to their large area.

707 **5.4.2 Clustering and tracking**

708 For events passing the quality selection cuts defined in section 5.4.1, the  $x$ - and  $y$ -coordinates  
709 of the ionization avalanche on each layer are extracted from the signal on the wires and strips  
710 respectively for each event, as shown schematically in figure 5.2. In this work,  $x$  is defined as  
711 the coordinate perpendicular to the wires and  $y$  is defined as the coordinate perpendicular  
712 to the strips. The  $z$ -coordinate is perpendicular to the sTGC surface.

713 The  $x$ -coordinate of the muon position is taken as the center of the wire group with the  
714 maximum peak signal amplitude, since the wire groups' pitch (36 mm) is larger than the  
715 typical extent of the ionization charge generated inside a sTGC. Assuming that the true  $x$ -  
716 position of the hit is sampled from a uniform distribution over the width of the wire group,  
717 the uncertainty in the  $x$ -position is approximately  $\frac{36}{\sqrt{12}}$  mm = 10 mm [64].

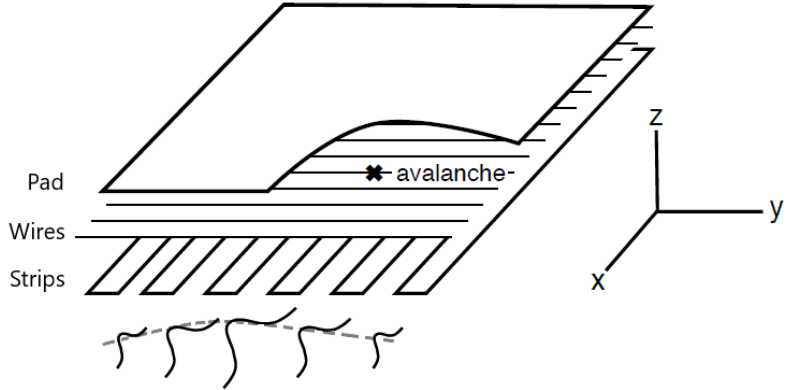


Figure 5.2: Schematic diagram representing the three types of electrodes in a sTGC detector. The position of the ionization avalanche is extracted from the wires and strips that picked up the avalanche signal. The signals on individual strips are sketched. Clustering is the process by which a Gaussian function (represented by the grey dashed line) is fitted to the distribution of the signal amplitude on individual contiguous strips; a sample cluster is shown in figure 5.3. In this work, the  $x(y)$ -coordinate will always refer to the coordinate perpendicular to the wires (strips). The  $z$ -coordinate is perpendicular to the sTGC surface [58, 56].

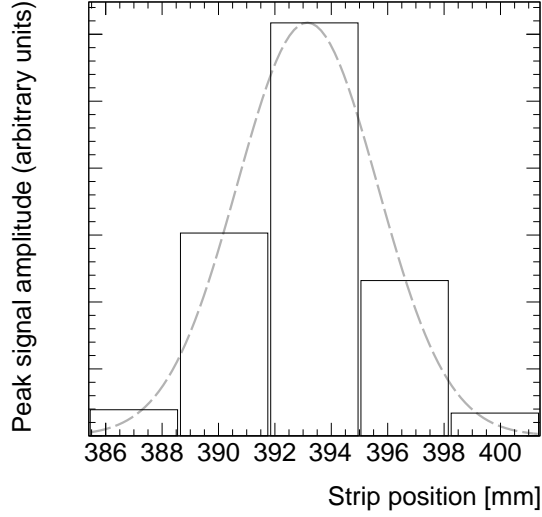


Figure 5.3: A sample cluster resulting from signal recorded on a group of contiguous strips after the passing of a muon. The grey dashed line represents the result of a fit to a Gaussian distribution.

718 The  $y$ -coordinate of the muon's position is taken as the Gaussian mean of the peak signal  
719 amplitude distribution across a group of contiguous strips that registered hits. The process  
720 of grouping contiguous strip hits on a layer is called clustering, and the resulting group is  
721 called a cluster. Figure 5.2 sketches the clustering process and a sample cluster is shown  
722 in figure 5.3. The data acquisition system recorded the identification number of the strip  
723 electrode that was hit and in the clustering process the position of the center of the strip  
724 electrode is calculated based on the nominal quadruplet geometry. Typically, clusters are  
725 built of 3-5 strips. The thickness of the graphite coating over the cathode boards determined  
726 how many strips picked up the ionization image charge. Larger clusters can often originate  
727 from  $\delta$ -rays since they spread the ionization charge over a larger area.

728 Events are removed from further analysis if there are two reconstructed clusters on one sTGC,  
729 since some hits could be from electronic noise or a simultaneous second muon traversing the  
730 chamber. Clusters are rejected if the cluster size is lesser than three strips (which should  
731 not happen for real events thanks to neighbour triggering), and if the cluster size is greater  
732 than 25. After all quality selection cuts are applied on hits and clusters, approximately half  
733 of the events recorded remain.

734 The uncertainty on the reconstructed cluster position is assessed by comparing the difference  
735 between Gaussian means obtained using two different algorithms. As shown in appendix A,  
736 the difference between the means from the two algorithms considered is found to be ap-  
737 proximately 60  $\mu\text{m}$  on average, larger than the statistical uncertainty on the Gaussian mean  
738 obtained from the cluster fit. Therefore, an uncertainty of 60  $\mu\text{m}$  is assigned to the recon-  
739 structed  $y$ -coordinate of a muon.

740 The reconstructed  $x$  and  $y$  coordinates on each quadruplet layer are used to reconstruct  
741 a straight track, independently, in the  $x$ - $z$  and  $y$ - $z$  planes. Tracks are reconstructed using  
742 muon coordinates for every possible pair of two sTGC layers. For example, if an event has  
743 muon coordinates reconstructed on all four layers, a total of six track segments in the  $x$ - $z$   
744 plane and six track segments in the  $y$ - $z$  plane will be reconstructed.

## 745 5.5 Relative local offsets

746 The offset of a strip from its nominal position can be modeled as a passive transformation.  
747 The *local offset* is defined as the shift in the strip pattern with respect to nominal geometry  
748 in a specific area of the sTGC. Local offsets systematically change the set of strips nearest  
749 to muons passing through an area. The data preparation software assumes that strips are  
750 in their nominal positions, so the recorded  $y$ -coordinate of the muon on layer  $i$ ,  $y_i$ , is shifted

751 opposite to the layer's local offset,  $d_{local,i}$ , by

$$y_i = y_{nom,i} - d_{local,i}, \quad (5.1)$$

752 where  $y_{nom,i}$  is the position of the muon that would have been recorded on layer  $i$  if there  
753 was no local offset. Equation 5.1 ignores other factors that affect the cluster position, like  
754 position resolution. With cosmics data, there was no external reference to measure  $y_{nom,i}$   
755 and the local offset is unknown. Therefore, only *relative* local offsets can be measured.

756 To measure relative local offsets, two of the four sTGC layers are chosen to provide a reference  
757 coordinate system. Relative local offsets are calculated with respect to the two reference  
758 or fixed layers. The hits on the two fixed layers were used to create tracks that can be  
759 interpolated or extrapolated (polated) to the other two layers. The set of two fixed layers  
760 and the layer polated to are referred to as a tracking combination. The residual of track  $i$ ,  
761  $\Delta_i$ , is defined as,

$$\Delta_i = y_i - y_{track,i}, \quad (5.2)$$

762 where  $y_{track,i}$  is the polated track position on the sTGC layer the residual is measured on.  
763 Track residuals are affected by the local offset in the area of each layer's hit. As an example,  
764 in figure 5.4, the residual on layer 2 perhaps indicates that layer 2 is offset with respect to  
765 layers 1 and 4 in the area of the track. Of course, a single track residual says nothing of  
766 the real relative local offset because of the limited spatial resolution of the detectors and  
767 fake tracks caused by noise or delta rays. However, the mean of residuals for all tracks in a  
768 region of interest will be shifted systematically by the local offsets between layers [58]. For  
769 a quadruplet with nominal geometry, the mean of residuals should be zero in all regions and  
770 for all reference frames, unlike the example regions in figure 5.5. The value of the mean of  
771 residuals is a measure of the relative local offset of the layer with respect to the two fixed  
772 layers used to reconstruct the muon track. The sign convention is such that the mean of  
773 residuals is opposite to the relative local offset.

774 To study the relative local offsets, residual distributions across each strip layer of a quadruplet  
775 for all possible tracking combinations are assembled and fitted. As expected, the residual dis-  
776 tributions are wider for tracking combinations where the extrapolation lever arm is largest,  
777 as in the example distributions shown in figure 5.5. In general, residual means from dis-  
778 tributions of residuals with geometrically less favourable tracking combinations have larger  
779 statistical and systematic uncertainties. The bin size of 200  $\mu\text{m}$  for the distributions shown  
780 in figure 5.5 was chosen based on the uncertainty on residuals calculated from tracks on layer  
781 4 (1) built from hits on layers 1 and 2 (3 and 4) given a cluster  $y$ -coordinate uncertainty  
782 of 60  $\mu\text{m}$  (discussed in section 5.4.2 and appendix A), since these tracks yield residuals with  
783 the largest uncertainties.

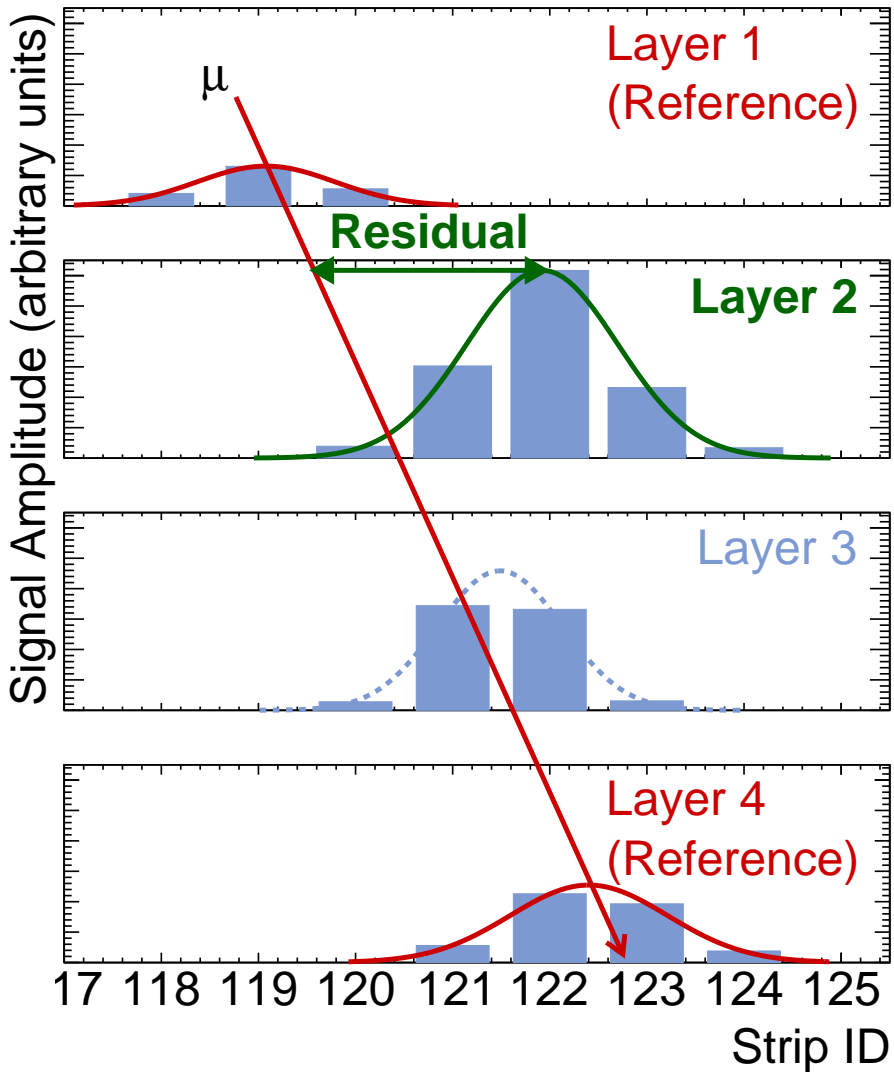
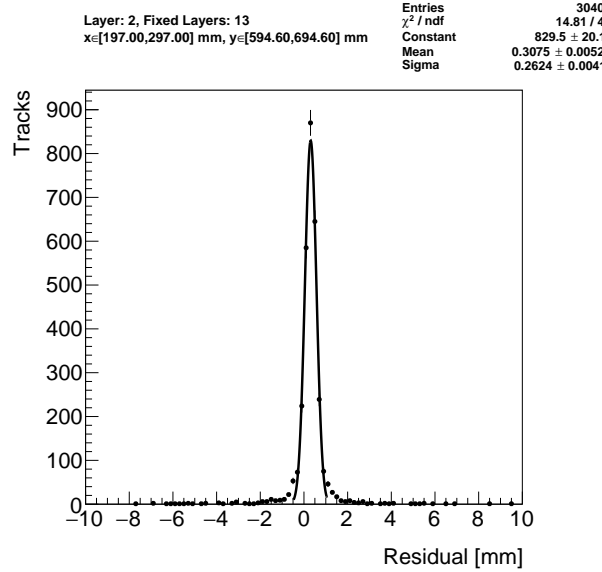
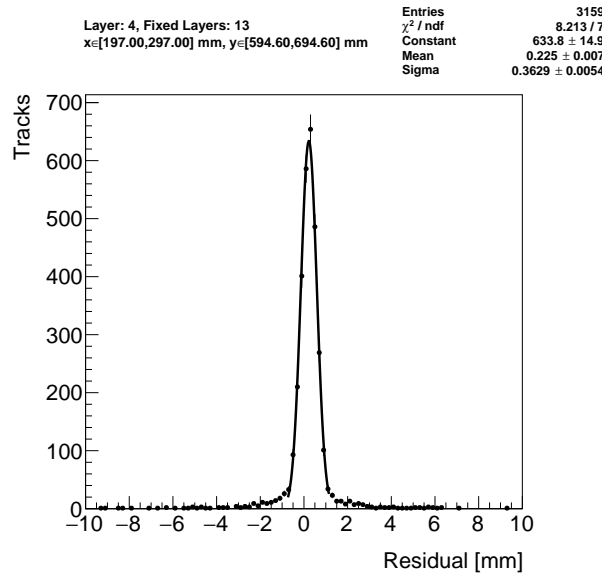


Figure 5.4: Representation of a muon event recorded by an sTGC quadruplet. The charge clusters measured using strip electrodes are fit with a Gaussian distribution and the fitted mean is taken as the reconstructed muon position. A track is built from the chosen reference layers, 1 and 4, and the track residual is calculated on layer 2. The clusters come from a real muon, but their positions were modified to highlight the non-zero value of the residual on layer 2.



(a) Tracks on layer 2, reference layers 1 and 3.



(b) Tracks on layer 4, reference layers 1 and 3.

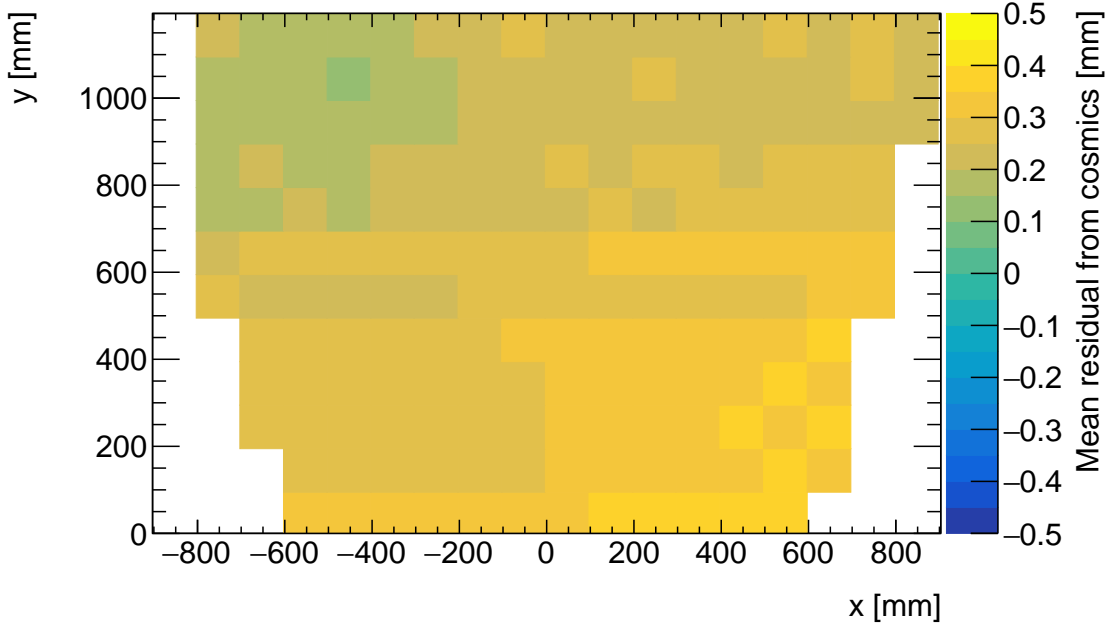
Figure 5.5: Residual distribution in the region  $x \in [197, 297]$  mm,  $y \in [594.6, 694.6]$  mm (100 mm by 100 mm area) for two different tracking combinations. Data from quadruplet QL2.P.11.

784 A Gaussian fit is used to extract the mean of the residual distributions. The residual distri-  
785 butions are actually better modeled by a double Gaussian distribution, which better captures  
786 the distribution tails in figure 5.5. However, a study described in appendix C.1 found that  
787 a fit to a single Gaussian function in the core of the distribution is sufficient to reconstruct  
788 the mean of the distribution.

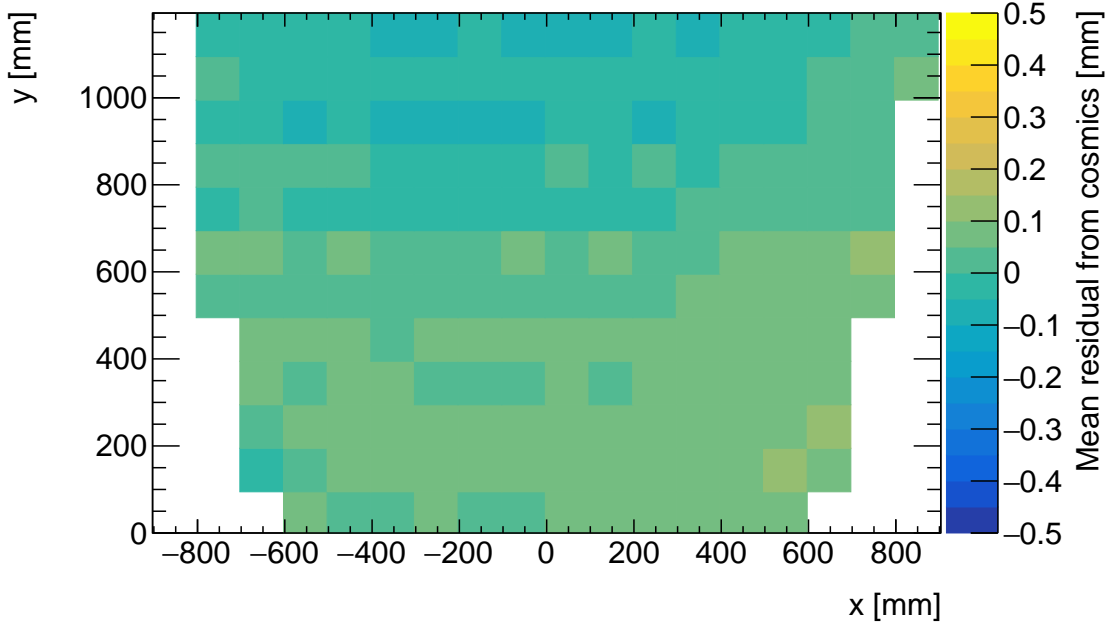
789 The area of the region of interest where tracks residuals were included in the residual distri-  
790 bution was 100 mm by 100 mm. The size balanced the number of tracks falling in the region  
791 of interest to give a small statistical uncertainty on the fitted mean while being smaller  
792 than the order on which local offsets were expected to change significantly. “Significantly”  
793 was defined as 100  $\mu\text{m}$ , the required position resolution of the sTGCs and the precision to  
794 which strip positions should be known. The distance over which local offsets are expected to  
795 change significantly can be estimated using a simple alignment model. Assuming the strips  
796 of a layer have been displaced uniformly from their nominal positions by a global offset and  
797 rotation, the distance in  $x$  that a large but possible rotation of 1 mrad changes the local  
798 offset by 100  $\mu\text{m}$  is 100 mm.

799 The means of residuals are plotted across each sTGC layer for every possible tracking combi-  
800 nation to get a picture of the how the relative local offsets change as a function of position  
801 over the layer’s surface. Figure 5.6 shows the mean of residuals on layer 2 calculated with  
802 layers 1 and 3 as reference for two different quadruplets, referred to as QL2.P.11 and QL2.P.8.  
803 In figure 5.6a, the Gaussian mean of the residual distribution in figure 5.5a is the entry in  
804 the bin defined by the boundaries  $x \in [197, 297]$  mm,  $y \in [594.6, 694.6]$  mm.

805 Many of the residual means are non-zero and change smoothly over layer 2, indicating that  
806 there are relative local offsets stemming from global misalignments between the strip patterns  
807 of different sTGC layers in both quadruplets. Given that the residual mean changes with  $x$  in  
808 figure 5.6a, quadruplet QL2.P.11 likely has a rotation of layer 2 with respect to layers 1 and  
809 3, combined with an offset of the entire layer. The residual means are smaller in figure 5.6b  
810 indicating that quadruplet QL2.P.8 is less misaligned overall than QL2.P.11; however, the  
811 relative local offsets range between  $\pm 200 \mu\text{m}$  so they are significant enough to warrant a  
812 correction so the quadruplet can achieve the required track angular resolution in the NSW.



(a) Mean of track residuals on layer 2, obtained using layers 1 and 3 as reference, for QL2.P.11.



(b) Mean of track residuals on layer 2, obtained using layers 1 and 3 as reference, for QL2.P.8.

Figure 5.6: Mean of residuals in each 100 mm by 100 mm bin over the area of sTGC layer 2 for quadruplets QL2.P.11 and QL2.P.8. The entry in  $x \in [197, 297]$  mm,  $y \in [594.6, 694.6]$  mm of figure 5.6a corresponds to the fitted Gaussian mean in figures 5.5a. The mean of residuals has the same value and opposite sign to the relative local offset of layer 2 with respect to the reference frame defined by layers 1 and 3.

## 813 5.6 Systematic uncertainty

814 The statistical uncertainty on the local residual means was typically around 10 - 20  $\mu\text{m}$ , and  
815 appendix B shows that the analysis is not statistically limited by the number of triggers  
816 collected for each quadruplet. Systematic uncertainties were found to be larger than the  
817 statistical uncertainty on the residual means.

818 Several analysis choices had some degree of impact on the fitted means of local track residual  
819 distributions. To study the impacts, the residual means were calculated in different ways and  
820 distributions of the differences made. The complete studies are shown in appendix C. The  
821 root-mean-square (RMS) of the residual mean difference distributions were used to quantify  
822 the impact of the different analysis choices as systematic uncertainties on the residual means.  
823 The following analysis choices are considered:

- 824 • The impact of performing a single or double Gaussian fit on the track residual distri-  
825 butions is studied. As shown in appendix C.1, the difference between fitting the track  
826 residual distribution with a single or double Gaussian function varies between 10-30  $\mu\text{m}$   
827 from the most to least geometrically favourable tracking combinations.
- 828 • The impact of the operating voltage used during data taking is investigated. Cosmic  
829 muon data was recorded at 2.9 kV and 3.1 kV. As described in appendix C.2, an  
830 uncertainty between 10-40  $\mu\text{m}$  is assigned to the different tracking combinations.
- 831 • The impact of using different Gaussian fitting algorithms used to reconstruct the po-  
832 sition of a charge cluster was considered. Clusters are fit with the Minuit2 [65] and  
833 Guo's method [66]. As shown in appendix C.3, the resulting difference in residual  
834 means is between 10-30  $\mu\text{m}$  from the most to least geometrically favourable tracking  
835 combinations.
- 836 • The impact of correcting reconstructed cluster positions for differential non-linearity  
837 (DNL) is studied. DNL is fully described in appendix C.4. It is a bias in the recon-  
838 structed cluster position that comes from discretely sampling a continuous distribu-  
839 tion, in this case the charge distribution [67, 58, 6]. The difference between residual  
840 means is compared with and without correcting the reconstructed cluster positions.  
841 Appendix C.4 shows that the impact of the correction is smaller than 10  $\mu\text{m}$  for all  
842 tracking combinations, which is almost negligible.

843 A summary of the systematic uncertainties assigned to the local means of residuals for each  
844 tracking combination is given in table 5.1. The RMS of the distributions of residual mean  
845 differences of geometrically similar tracking combinations are averaged and the average value

Tracking geometry	Residual distribution fit function (C.1)	Cosmics data collection voltage (C.2)	Cluster fit algorithm (C.3)	Apply DNL correction or not (C.4)	Total
Similar to layer 3, fixed layers 1, 2	0.01 mm	0.04 mm	0.02 mm	0.01 mm	<b>0.05 mm</b>
Similar to layer 4, fixed layers 1, 2	0.03 mm	0.01 mm	0.03 mm	0.01 mm	<b>0.10 mm</b>
Similar to layer 2, fixed layers 1, 3	0.01 mm	0.02 mm	0.01 mm	0.000 mm	<b>0.03 mm</b>
Similar to layer 4, fixed layers 1, 3	0.01 mm	0.04 mm	0.01 mm	0.01 mm	<b>0.04 mm</b>
Similar to layer 2, fixed layers 1, 4	0.01 mm	0.04 mm	0.01 mm	0.01 mm	<b>0.04 mm</b>

Table 5.1: Systematic uncertainty assigned for each analysis option, detailed in appendix C.

846 is taken as the systematic uncertainty for those tracking combinations. An example of a ge-  
 847 ometically similar pair of tracking combinations is fixing layers 1 and 2 and extrapolating  
 848 to layer 3 or fixing layers 2 and 3 and extrapolating to layer 4; geometrically similar combi-  
 849 nations have the same polation lever arm. The total systematic uncertainty is obtained by  
 850 summing in quadrature all the different sources of systematic uncertainty. The uncertainty  
 851 in each mean of residuals is obtained by summing in quadrature the statistical uncertainty  
 852 in the mean of residuals and the appropriate systematic uncertainty for the tracking com-  
 853 bination used to calculate the mean of residuals.

## 854 5.7 Discussion

855 The total uncertainty in the residual means, and hence the relative local offsets, is typically  
 856 less than the design sTGC position resolution of  $\sim 100 \mu\text{m}$  [5]. Therefore, the residual means  
 857 are relevant input for alignment studies.

858 The relative local offsets calculated from the means of residual distributions over the surface  
859 of an sTGC layer for all tracking combinations provide a complete picture of the relative  
860 alignment between sTGC layers in a quadruplet module. In fact, cosmic muon testing is the  
861 only characterization technique where the entire surface of quadruplet layers can be probed  
862 since muons hits are distributed almost uniformly; the CMM [7] and x-ray methods [8]  
863 depend on measurements at reference points, and test beams only have a limited beam spot  
864 to work with [6]. By looking at 2D-histograms of residual means like figure 5.6 for all tracking  
865 combinations, it is easy to identify quadruplets that suffer large relative misalignment since  
866 many residual means differ significantly from zero. Moreover, the pattern in the residual  
867 means can be used to motivate a physical interpretation of misalignments. The residual  
868 means can be used as a reference, cross check, or input to other alignment studies.  
869 Relative local offsets cannot be used to position strips in the absolute ATLAS coordinate  
870 system because there is no external reference to measure positions on all layers with respect  
871 to. The lack of an external absolute reference frame means that there is not enough infor-  
872 mation to unfold relative local offsets into absolute local offsets (with respect to the nominal  
873 quadruplet geometry). As an example, assuming that the residual on layer 2 in figure 5.4 is  
874 representative of the absolute value of the relative local offset, the residual on layer 2 could  
875 be caused by the strips on layer 2 being misaligned from nominal, but it could also be caused  
876 by strips on layers 1 and 4 being offset from nominal while the strips on layer 2 are in their  
877 nominal positions! Any number of combinations of local offsets on layers 1, 2 and 4 could  
878 produce the residual on layer 2. Absolute local offsets must be calculated using another  
879 method: the x-ray method.

880 **Chapter 6**

881 **Using x-rays to measure relative strip  
882 position offsets**

883 This chapter describes the analysis of x-ray data to measure relative local strip position  
884 offsets, which can be compared with results obtained using cosmic data. The reader is re-  
885 ferred to the paper describing the x-ray method [8]. Some minor changes to the experimental  
886 setup have been made since the paper was written. The experimental setup described here  
887 is current and was used to collect the data presented in this thesis.

888 **6.1 Experimental setup**

889 The x-ray tests were performed after the quadruplets had arrived at CERN, had been were  
890 assembled into wedges, and the alignment platforms installed. An x-ray gun was attached to  
891 one of the alignment platforms glued to the surface of the wedge and the x-ray beam profile  
892 was recorded by the strip electrodes.

893 The sTGC wedges were installed on carts that could rotate their surface to a horizontal  
894 position. A mounting platform was installed on top of the alignment platform using a three-  
895 ball mount. The x-ray gun used was an Amptek Mini-X tube [68]. The x-ray gun was placed  
896 in a brass holder with built-in 2 mm collimator and 280  $\mu\text{m}$  copper filter. The holder was  
897 mounted on one of five positions on the mounting platform, as shown in figure 6.1. The  
898 x-ray gun positions were chosen to avoid wire support structures in the sTGCs that reduce  
899 hit efficiency [58] and boundaries between sets of strips read out by two different ASICs that  
900 could each have different thresholds.

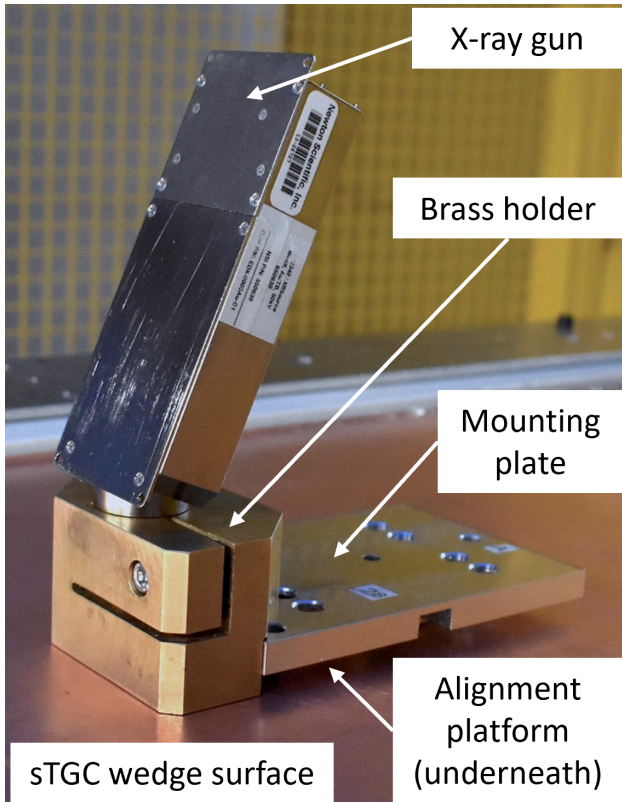


Figure 6.1: The x-ray gun mounted to an alignment platform on the surface of a sTGC wedge. Adapted from [8].

- 901 As with cosmics data collection, each sTGC also needed gas and high voltage to operate.  
 902 Each sTGC layer was operated at 2.925 kV with high voltage from a NIM crate. The sTGC  
 903 gas volumes were flushed with CO<sub>2</sub> before and during data collection. The sTGCs were not  
 904 operated using the nominal pentane-CO<sub>2</sub> gas mixture due to constraints in its availability  
 905 based on safety concerns. The sTGC efficiency is significantly lower when operated with  
 906 only CO<sub>2</sub>.  
 907 The gun produced x-rays with energies under 40 keV with peaks in the 7-15 keV range. Peaks  
 908 in the 0-30 keV range were filtered out by the copper filter and the copper of the sTGCs. The  
 909 x-rays mostly interacted with the sTGC wedge's copper electrodes and gold-plated tungsten  
 910 wires via the photoelectric effect. The resulting photoelectrons that enter the gas volume  
 911 caused ionization avalanches which were picked up by the readout strips.

912 **6.2 Data acquisition**

913 A different version of the same front end electronics, but the same ASIC, as used in cosmics  
914 testing were used for the x-ray testing to measure the peak signal amplitude. Data was  
915 collected for two minutes per gun position with random triggers. A trigger recorded all  
916 signals above threshold. Pad and wire data was not recorded.

917 **6.3 Data preparation**

918 Following a similar approach to the cosmics data analysis described in chapter 5, a default  
919 pedestal is subtracted from the signal peak amplitude on each electrode.

920 Clusters are defined as groups of contiguous strip hits recorded within 75 ns. The distribution  
921 of peak signal amplitude from continuous strip hits is fitted with a Gaussian function, and the  
922 mean of the fitted Gaussian is taken as the cluster position. Cluster positions are corrected  
923 for differential non linearity (or DNL, see definition in appendix C.4). Although the impact  
924 of the DNL correction on the reconstructed cluster means is small, it is important to improve  
925 the spatial resolution of the sTGC strip layer. Only clusters composed of hits on 3-5 strips  
926 are used in the x-ray analysis. Clusters with signal on more than five strips are cut because  
927 they were most likely caused by photoelectrons ejected with enough energy to cause more  
928 primary ionization and subsequent avalanches as  $\delta$ -rays.

929 The x-ray analysis diverges entirely from the cosmics analysis algorithm here because the  
930 ionization from x-rays does not originate from one charged particle traversing all layers  
931 of a sTGC quadruplet, so there is no track to rebuild. Rather, ionization avalanches [54]  
932 are generated by photoelectrons liberated from the metals of the sTGCs, which only travel  
933 through one gas volume and are produced at all angles. Instead of reconstructing a straight  
934 line trajectory through multiple sTGC layers, the cluster position distribution on each sTGC  
935 layer is used to reconstruct the beam profile. A typical x-ray beam profile is shown in  
936 figure 6.2.

937 **6.4 Measuring local offsets**

938 The fitted Gaussian mean of the cluster position distribution is taken as the reconstructed  
939 center of the x-ray beam profile on each sTGC layer. The reconstructed center is compared to  
940 the expected beam profile center, calculated in two steps. First, the position of the alignment  
941 platform with respect to the brass inserts and the nominal position of the strips under the

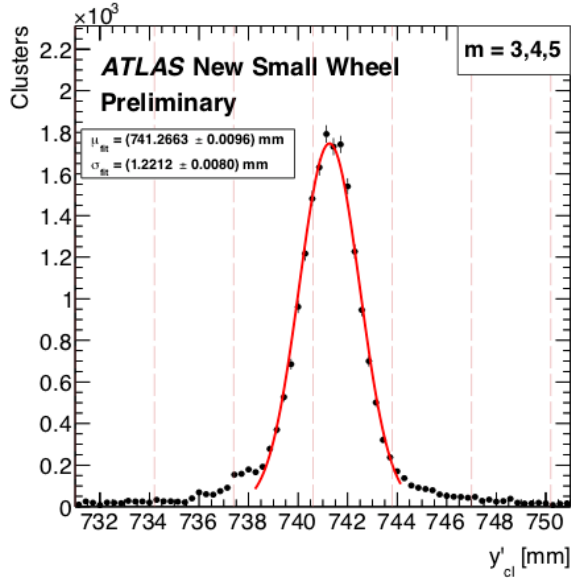


Figure 6.2: An example distribution of x-ray cluster mean positions after the analysis selection cuts and DNL corrections are applied. The strip cluster multiplicity,  $m$ , was limited to 3, 4 or 5. The red curve is a Gaussian fit of the distribution and the pink dashed lines denote the edges of the strips [8].

942 gun position with respect to the brass inserts are used to calculate the expected beam profile  
 943 center assuming a nominal quadruplet geometry. Second, the expected beam profile center  
 944 is corrected for the geometry of the brass holder, the positioning and angle of the alignment  
 945 platforms, and the beam angle. The difference between the expected and reconstructed beam  
 946 profile centers is a measure of the local offset of the strip electrode pattern. Applying the  
 947 logic of equation 5.1 to the beam profile, the Gaussian mean of cluster positions on the given  
 948 layer acts as the recorded position,  $y_i$ , the expected center is  $y_{nom,i}$  and the local offset is  
 949  $d_{local,i}$  as before, where  $i$  denotes the layer. Since the position of the alignment platforms will  
 950 be monitored continuously by the alignment system in ATLAS [5], the position of the strips  
 951 that should have been at the x-ray gun position are shifted by  $d_{local,i}$  and so their absolute  
 952 positions in the ATLAS coordinate system are known for every position where x-ray data  
 953 was recorded. Therefore, the x-ray local offsets can be used to measure the position of  
 954 some strips in the ATLAS coordinate system, as is required for the triggering and precision  
 955 tracking goals of the NSWs as discussed in chapter 4.

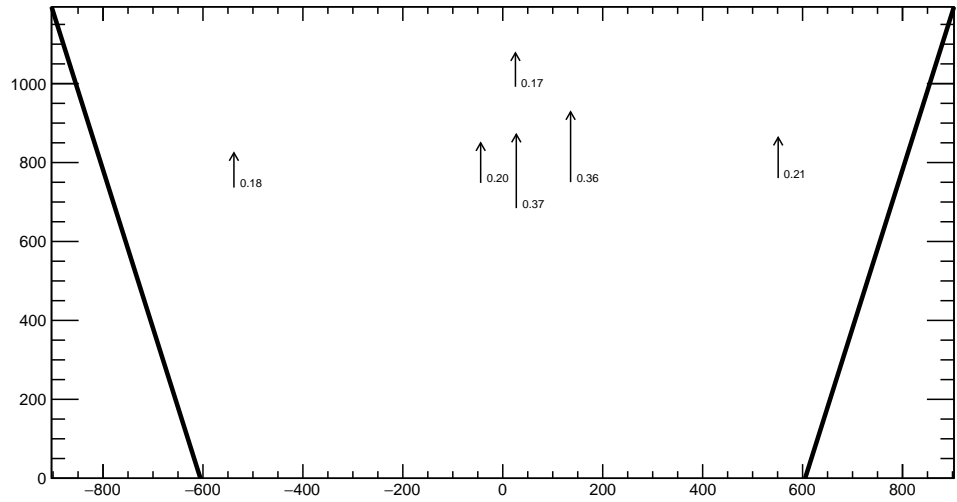
956 Studies of systematic effects on the measured beam profile centers lead the x-ray working  
 957 group to accept an uncertainty of 120  $\mu\text{m}$  on the beam profile centers. The largest uncertainty

958 comes from the effect of the gun angle, which proved difficult to measure and correct for.  
959 The details and results of the systematics studies have not been published externally.  
960 The absolute local strip offsets measured using the method described above are not presented  
961 here as the author did not conduct this work. However, the author used the *absolute* local  
962 offsets to calculate *relative* local offsets that can be compared to the relative local offsets  
963 measured using cosmic muon data.

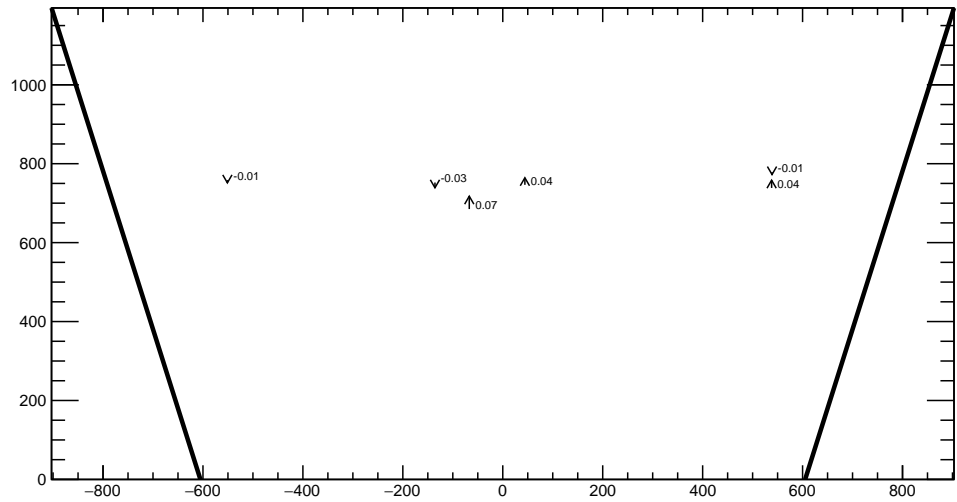
## 964 6.5 Measuring relative local offsets

965 The novelty of the x-ray method and the uncertainty in the x-ray local strip position offsets,  
966 which greater than the precision to within which the position of the strips would ideally be  
967 known, means that the x-ray local offsets should be validated by an independent method.  
968 Absolute local offsets measured using x-ray data and relative local offsets measured using  
969 cosmics data cannot be compared directly because they are not defined with respect to the  
970 same coordinate system: x-ray absolute local offsets are measured in the ATLAS coordinate  
971 system while cosmics relative local offsets are defined with respect to a reference frame  
972 established by two sTGC layers in a quadruplet. The following describes the method used to  
973 calculate relative local strip position offsets from the x-ray local offsets that can be compared  
974 to the cosmics relative strip position offsets.

975 Given that the measured x-ray beam profile centers are systematically affected by local strip  
976 position offsets in the same way as the means of the cosmic ray track residual distributions,  
977 the x-ray beam profile centers on each sTGC layer are used to reconstruct a straight line in  
978 the  $y$ - $z$  plane using the beam profile centers on two sTGC layers chosen as reference, in a  
979 manner similar to the track reconstruction performed with cosmic muon data. A residual  
980 is calculated as the difference between the beam profile center on the layer of interest and  
981 the polated straight line fitted from two sTGC layers taken as a reference. The beam profile  
982 center on the layer of interest acts as  $y_i$  and the polated track position acts as  $y_{track,i}$  in  
983 equation 5.2. As with the means of cosmic track residual distributions, the sign convention  
984 is such that the x-ray residual is opposite in sign to the relative local offset of the layer of  
985 interest with respect to the two fixed layers.



(a) X-ray residuals on quadruplet QL2.P.11 layer 2 obtained using reference layers 1 and 3.



(b) X-ray residuals on quadruplet QL2.P.8 layer 2 obtained using reference layers 1 and 3.

Figure 6.3: The x-ray residuals on sTGC layer 2 calculated with respect to the beam profile centers on sTGC layers 1 and 3 for quadruplet QL2.P.11 (a) and QL2.P.8 (b). The arrows originate from the expected position of the beam profile center assuming a nominal geometry. The lengths of the arrows are 500 times the value of the x-ray residuals, scaled for visibility. The value of the x-ray residuals are annotated in millimeters and have an uncertainty of  $\pm 0.15$  mm.

986 For each x-ray survey position, the x-ray residuals were calculated for all possible pairs of  
987 sTGC layers taken as reference and each sTGC layer the straight line could be polated to, as  
988 was done for cosmic muon tracks. Calculating a residual required x-ray beam profiles on at  
989 least three layers. Figure 6.3 shows the x-ray residual values on sTGC layer 2 with respect to  
990 reference layers 1 and 3 for sTGC quadruplet modules QL2.P.11 and QL2.P.8. For module  
991 QL2.P.11, a negative relative local offset is measured at all x-ray survey points, indicating a  
992 global translation of sTGC layer 2 with respect to layers 1 and 3.  
993 The uncertainty on the x-ray residualsis is obtained by propagating the uncertainty on the  
994 reconstructed x-ray beam profile centers ( $120\text{ }\mu\text{m}$ ) through the polation. The uncertainty  
995 on the x-ray residuals ranges from  $150\text{ }\mu\text{m}$  to  $400\text{ }\mu\text{m}$  from the most to least geometrically-  
996 favourable tracking combination. There is no discernible pattern of misalignmnet revealed by  
997 the x-ray residuals on QL2.P.8 because they have absolute values smaller than the uncertainty  
998 on the x-ray residuals ( $150\text{ }\mu\text{m}$ ).  
999 The relative local offsets calculated using cosmics data and x-ray data will be compared in  
1000 the next chapter.

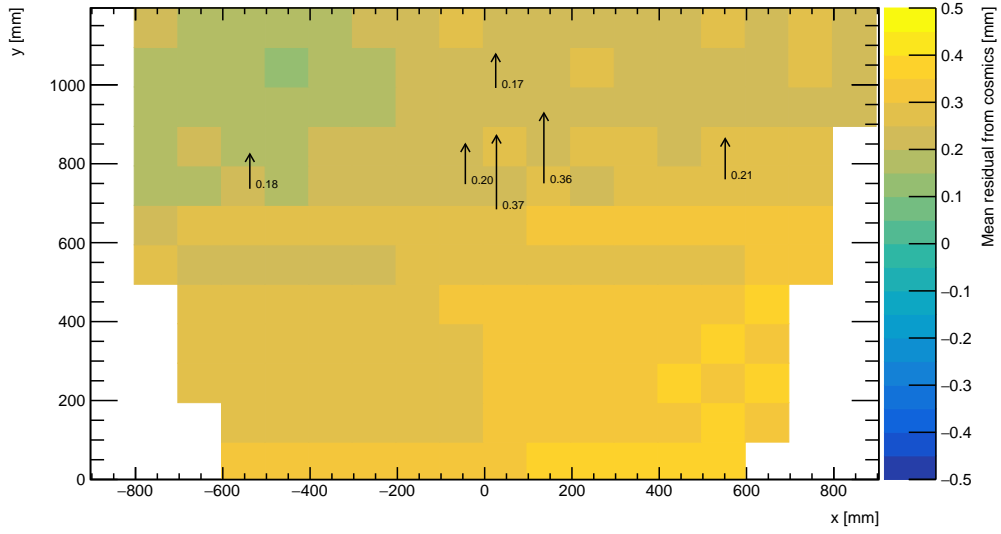
1001 **Chapter 7**

1002 **Comparing cosmic muon and x-ray  
1003 relative strip position offsets**

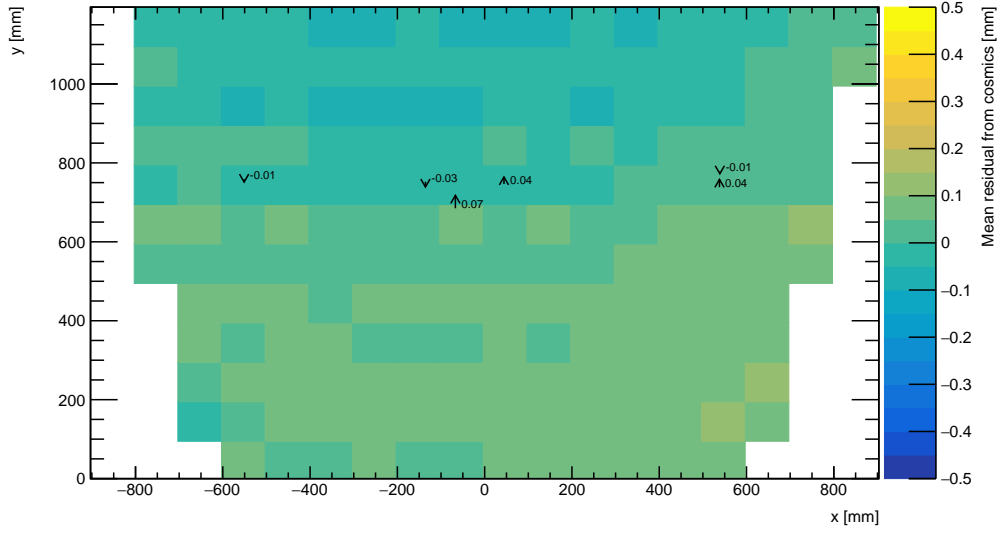
1004 The goal of the work presented in this thesis is to validate the local strip position offsets  
1005 measured with x-ray data with results obtained using cosmic ray data. The challenge was  
1006 that the x-ray dataset provided absolute local offsets measured in the ATLAS coordinate  
1007 system while the cosmics dataset provided relative local offsets measured with respect to a  
1008 reference frame defined by two of four sTGC layers in a quadruplet – which could not be  
1009 compared directly. To address the challenge, the x-ray local offsets were used to calculate  
1010 relative local offsets. Relative local offsets on each sTGC layer obtained with x-ray and  
1011 cosmics data calculated using the same two sTGC reference layers are compared for each  
1012 area where x-ray data is available. The results of the comparison are presented here.

1013 **7.1 Results**

1014 Relative local offsets have the same value but opposite sign to the mean cosmics and x-ray  
1015 residuals. For the remainder of this chapter, the means of cosmic track residual distributions  
1016 will be referred to as mean cosmics residuals.  
1017 Mean cosmics and x-ray residuals on sTGC layer 2 calculated with reference layers 1 and 3  
1018 across the quadruplet surface are shown in figure 7.1 for sTGC quadruplets QL2.P.11 and  
1019 QL2.P.8. Figure 7.1 is a superposition of figures 5.6 and 6.3.



(a) Mean cosmics and x-ray residuals on sTGC layer 2 of quadruplet QL2.P.11 obtained using reference layers 1 and 3.



(b) Means cosmics and x-ray residuals on sTGC layer 2 of quadruplet QL2.P.8 obtained using reference layers 1 and 3.

Figure 7.1: The mean cosmics residuals are shown using colour. The x-ray residuals available at nominal gun positions are drawn as arrows and the value of the residual annotated in millimeters with uncertainty  $\pm 0.15$  mm. The length of the arrows is 500 times the value of the x-ray residual, scaled for visibility. These plots are a superposition of figures 5.6 and 6.3.

1020 Figure 7.1a shows that for QL2.P.11 the x-ray residuals are of the same sign and order as  
1021 the mean cosmics residuals, as can be seen by comparing the annotated value of the x-ray  
1022 residual to the mean cosmics residual represented in the nearest coloured bin. QL2.P.11's  
1023 mean cosmics and x-ray residuals are correlated.

1024 For QL2.P.8, figure 7.1b shows that the x-ray residuals are of the right order compared to the  
1025 mean cosmics residuals; however, the value of the x-ray residuals are within their uncertainty  
1026 so the correlation is not manifest. While the x-ray residuals do not reveal a pattern in the  
1027 relative local offsets across the layer's surface, the mean cosmics residuals show a structure  
1028 to the relative local offsets, revealed by how they vary smoothly over the surface of sTGC  
1029 layer 2.

1030 The comparison of mean cosmics and x-ray residuals was done for several sTGC quadruplets  
1031 for all possible tracking combinations. Scatter plots of the x-ray and mean cosmics residuals  
1032 on QL2.P.11 and QL2.P.8 for all tracking combinations are shown in figures 7.2 and 7.3  
1033 and reveal the degree of correlation between the datasets. In these correlation plots, each  
1034 rectangle is centered on the value of a mean cosmics and x-ray residual pair calculated with a  
1035 given tracking combination for every x-ray gun position where data is available. The height  
1036 and width of the rectangles are the uncertainty in the mean cosmics and x-ray residuals  
1037 respectively. Note that in the scatter plots, the regions of interest where cosmics tracks are  
1038 included in the calculation of the mean of residuals are exactly centered on the nominal x-ray  
1039 beam positions, unlike in figure 7.1.

1040 The fitted slope and offset in figure 7.2 show that the two QL2.P.11 datasets are correlated.  
1041 The large uncertainty on the x-ray residuals set a limit on the sensitivity of the analysis,  
1042 for if the absolute value of the x-ray residuals of a quadruplet were smaller than the x-ray  
1043 residual uncertainties, no conclusion about the correlation could be drawn, as is the case for  
1044 layer 2 of sTGC quadruplet QL2.P.8 (figure 7.3). This result is reflected in the small x-ray  
1045 residuals shown in figure 7.1b that do not reveal a pattern in the relative local offsets across  
1046 the surface of sTGC layer 2. However, figure 7.3 shows that the x-ray and mean cosmics  
1047 residuals are clustered approximately around zero as is expected for a quadruplet with small  
1048 relative misalignments between layers.

1049 There are three patterns in the residuals on the scatter plot explained by geometry. First,  
1050 for both datasets the uncertainty in the extrapolated track residuals were larger than the  
1051 interpolated track residuals because of the extrapolation lever arm. For the x-ray residuals,  
1052 the effect of the lever arm on the uncertainty was direct since the residual was calculated  
1053 from a single straight line; for the mean cosmics residuals it is the widening of the residual  
1054 distributions due to the extrapolation lever arm that increases the uncertainty in the fitted  
1055 means of residuals. Second, residuals calculated through extrapolation tend to be larger  
1056 because the extrapolation lever arm can produce more extreme values of the track position

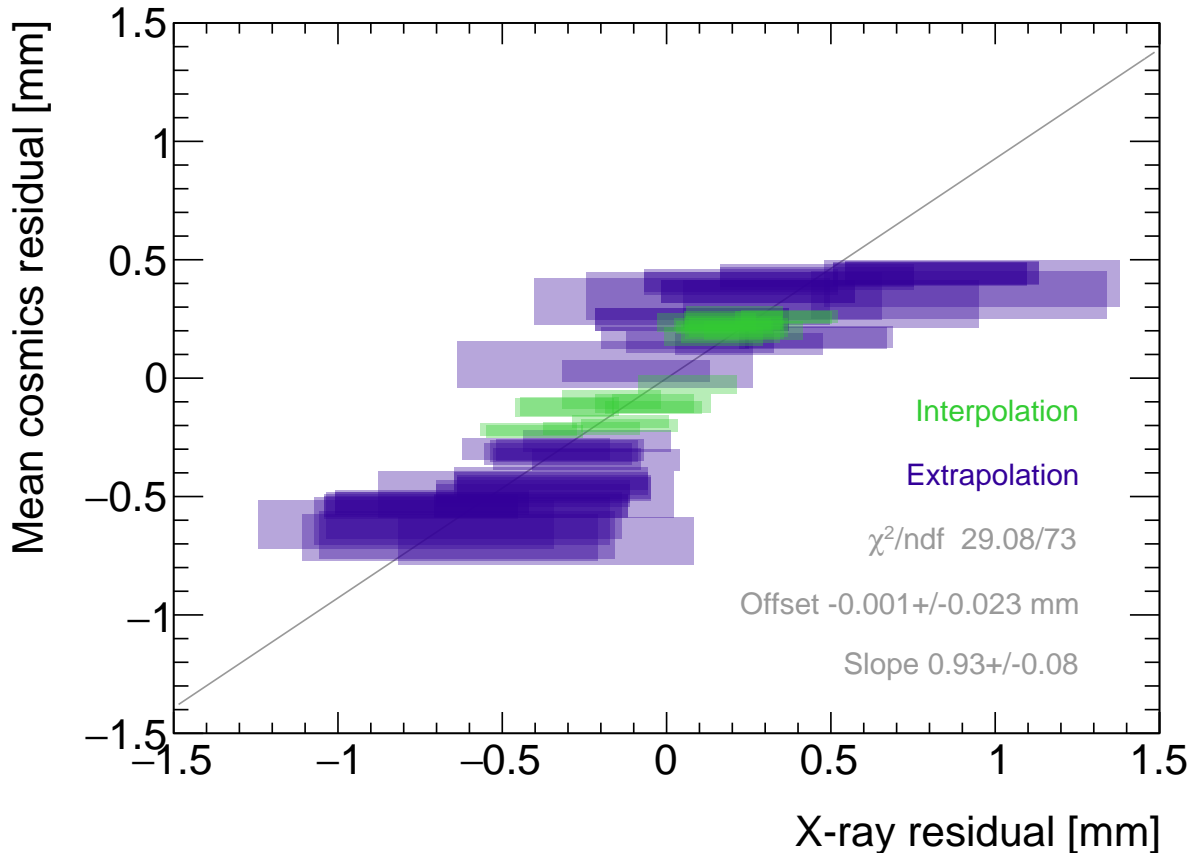


Figure 7.2: Correlation plot between x-ray and mean cosmics residuals for all tracking combinations for QL2.P.11. Each rectangle is centered on an x-ray and mean cosmics residual pair calculated at a given x-ray gun position and for a certain tracking combination. The width of the rectangles in  $x$  and  $y$  are the uncertainty in the x-ray and mean cosmics residual respectively. A printer-friendly version of this plot is available in appendix D.

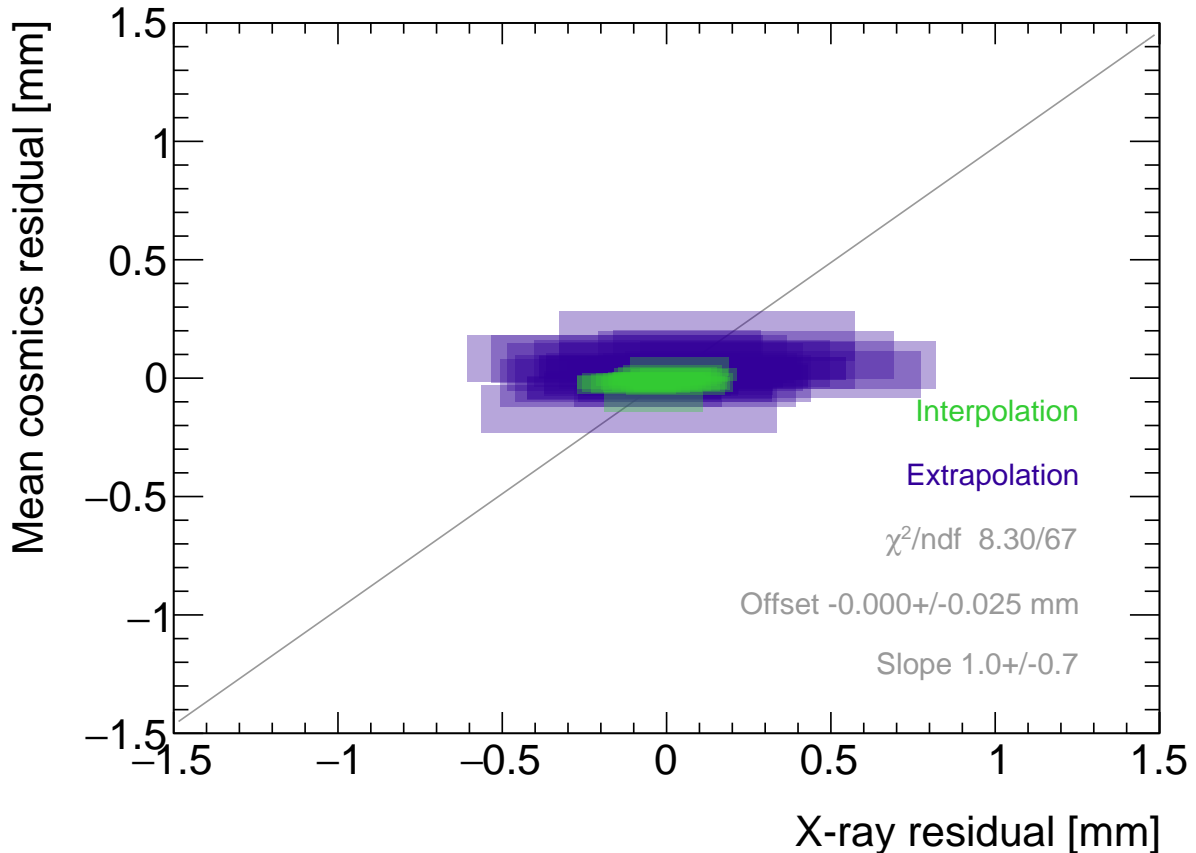


Figure 7.3: Correlation plot between x-ray and mean cosmics residuals for all tracking combinations for QL2.P.8. Each rectangle is centered on an x-ray and mean cosmics residual pair calculated at a given x-ray gun position and for a certain tracking combination. The width of the rectangles in  $x$  and  $y$  are the uncertainty in the x-ray and mean cosmics residuals respectively. A printer-friendly version of this plot is available in appendix D.

on the layer of interest. Third, the points in figure 7.2 are geometrically correlated (e.g. they seem to be roughly mirrored around the origin). This is expected since the residuals calculated using a given set of three layers should be geometrically correlated by the local offsets on each layer (the  $d_{local,i}$  on each layer as defined in equation 5.1).

## 7.2 Discussion

Several sTGC quadruplets were tested for each quadruplet construction geometry built in Canada. Each quadruplet fell into one of the two categories: residuals large enough to see a correlation, or residuals too small to see a correlation. Since the x-ray and mean cosmics residuals can be used to calculate relative local offsets between the layer and the two reference layers, quadruplets with the largest relative misalignments had the largest range of residuals. The correlation plots are another easy visual way to identify quadruplets with large relative misalignments.

The most significant limit on measuring the degree of correlation between the x-ray and mean cosmics residuals is the uncertainty on the x-ray residuals, which stemmed from the systematic uncertainty of 120  $\mu\text{m}$  in the x-ray beam profile centers used to construct the straight lines. For example, in figure 7.3, if the x-ray residuals could be known to within better precision, perhaps they would be correlated with the mean cosmics residuals. The x-ray method was limited primarily by the systematic uncertainties in the relative alignment of the alignment platforms and the gun, especially the gun angle.

The analysis of a fraction of the sTGC quadruplets was limited by the availability of data. Sometimes, less than three sTGC layers in a quadruplet were surveyed for a given x-ray gun position so no residuals could be calculated. Too few x-ray residuals prevented the analysis from detecting a significant correlation with cosmics data, should it even be measurable. Often, the analysis of sTGC quadruplets of smaller sizes (placed innermost on the wheel) is limited because they have fewer alignment platforms, and hence gun positions, on their surfaces as a result of their size. The analysis is also limited to a fraction of all sTGC quadruplets built. The wedges constructed the earliest (typically small wedges) were surveyed when the x-ray method was still being designed, so a limited number of x-ray residuals can be calculated and the beam profiles were of lower quality.

Nonetheless, the comparison of x-ray and mean cosmics residuals was really to confirm the x-ray method's ability to measure local offsets with an independent dataset. The x-ray local offsets allow the calculation of relative local offsets that have been correlated to the cosmics relative local offsets. Therefore, the analysis of quadruplets with relative local offsets large enough to detect a correlation validates the x-ray method's ability to measure local offsets.

1091 The potential of using relative local offsets calculated from cosmics data to study relative  
 1092 alignment between sTGC layers stands on its own. For example, although the x-ray residuals  
 1093 in QL2.P.8 in figure 7.1b do not reveal a pattern, the variation in the mean cosmics residuals  
 1094 do. Identifying the pattern is possible because mean cosmics residuals can be calculated  
 1095 across the entire sTGC layer's area and are sensitive to smaller relative local offsets since  
 1096 their uncertainty is significantly smaller.

## 1097 7.3 Next steps

1098 The results presented in this thesis pave the way to the further application of the rich cosmic  
 1099 muon data set to alignment work. First, a systematic study of cosmic ray and x-ray relative  
 1100 local strip position offsets should be performed for all quadruplets built for the NSWs. The  
 1101 correlation plots such as those presented in figure 7.2 and 7.3 can reveal unexpected results  
 1102 which could indicate an issue with either cosmic ray or x-ray data collection to be investigated  
 1103 further. Then, the overall correlation between x-ray and cosmic datasets should be quantified  
 1104 for all quadruplets instead of being quantified for each quadruplet individually.

1105 For now, the correlation of the individual quadruplets tested supports the use of the x-  
 1106 ray data to build an alignment model. The plan is that the alignment parameters will  
 1107 be provided to the ATLAS experiment's offline software to estimate the position of each  
 1108 strip and so improve precision muon tracks reconstruction using the sTGCs. Work on the  
 1109 alignment model is ongoing [8]. Currently, the algorithm compares the offsets of a local  
 1110 group of strips at each x-ray gun position as measured by the x-ray and CMM methods  
 1111 in a fit to extract a global slope ( $m$ ) and offset ( $b$ ) per layer,  $i$ , where the  $\chi^2$  is given by  
 1112 equation 7.1.

$$\chi^2 = \frac{[dy_{cmm,corr} - dy_{xray}]^2}{\delta dy_{xray}^2 + \delta dy_{cmm,corr}^2}, \quad (7.1)$$

$$dy_{cmm,corr} = y_{cmm} + b_i + m_i x - y_{nom} \quad (7.2)$$

1113  
 1114 Here,  $dy$  is a local strip position offset as calculated from the x-ray and corrected CMM  
 1115 data and  $\delta dy$  refers to their respective uncertainties. The large uncertainty on the x-ray  
 1116 local offsets (120  $\mu\text{m}$ ) and the sparseness of the measurements means that including input  
 1117 from other characterization datasets could reduce the uncertainty on the alignment model  
 1118 parameters.

1119 Work on adding the relative local strip position offsets measured using cosmic ray data to the  
1120 alignment model has begun. They provide alignment information between the x-ray measure-  
1121 ment points and can be calculated with a precision relevant to alignment studies. Therefore,  
1122 they provide additional and complementary information that could further constrain the  
1123 global rotation and translation parameter of the simple misalignment model currently being  
1124 used. It is compelling to imagine improving the accuracy of the alignment model given that  
1125 the accuracy to which the positions of the strips are known in ATLAS will affect the quality  
1126 of the reconstructed muon tracks used to study high energy physics processes.

<sub>1127</sub>

# Chapter 8

<sub>1128</sub>

## Summary and outlook

<sub>1129</sub> The LHC [1] will be at the energy frontier of particle physics for at least the next decade,  
<sub>1130</sub> making it a unique tool with which to study particle physics. With the HL-LHC [2], high  
<sub>1131</sub> statistics on rare particle physics processes will enable more precise measurements of pa-  
<sub>1132</sub> rameters of the Standard Model and increase the sensitivity to signatures of physics beyond  
<sub>1133</sub> the Standard Model [3]. To capitalize on the increased luminosity, the muon small wheels  
<sub>1134</sub> of the ATLAS experiment must be replaced to keep the current triggering and tracking  
<sub>1135</sub> performance [5].

<sub>1136</sub> sTGCs are gas ionization chambers optimized for a high rate environment [5]. Using the pad  
<sub>1137</sub> electrodes to define a region of interest makes it possible to get track segments of  $\sim 1$  mrad  
<sub>1138</sub> angular resolution quickly, which will be used as input to check if a collision originated  
<sub>1139</sub> from the interaction point and whether it should be triggered on [5, 53]. Thanks to the  
<sub>1140</sub> careful design of the sTGCs, particularly the small pitch of the strip readout electrodes, the  
<sub>1141</sub> sTGCs are able to provide better than  $100 \mu\text{m}$  position resolution per detector plane to fulfill  
<sub>1142</sub> precision offline tracking requirements [6].

<sub>1143</sub> Ultimately, the positions of the sTGC strip electrodes need to be known in ATLAS to within  
<sub>1144</sub>  $\sim 100 \mu\text{m}$  so that they can deliver the required position resolution [5]. The strategy is to build  
<sub>1145</sub> an alignment model to estimate the position of each strip [8]. Input to the alignment model  
<sub>1146</sub> comes from the datasets used to characterize the quadruplets. The x-ray data [8] is the only  
<sub>1147</sub> characterization dataset that directly links the position of the strips to the ATLAS coordinate  
<sub>1148</sub> system. The alignment model could be built on x-ray data alone, but the sparseness of and  
<sub>1149</sub> large uncertainty on the local offsets mean that the alignment model could benefit from more  
<sub>1150</sub> input. The x-ray method is also a new technique that should be independently validated.

<sub>1151</sub> Relative local offsets measured with the cosmics and x-ray datasets were compared and the  
<sub>1152</sub> observed correlation confirmed the local offsets measured with the x-ray gun. Moreover, the

1153 cosmics relative local offsets are useful on their own. The 2D visualizations of relative local  
1154 offsets make it possible to quickly identify areas of misaligned strips and make hypotheses as  
1155 to the physical origin of those misalignments. Also, the cosmics residual means were shown  
1156 to be robust and have uncertainties under 100  $\mu\text{m}$  for all two-fixed-layer reference frames,  
1157 which is small in this context. Therefore, the cosmics relative local offsets complement the x-  
1158 ray data by providing a complete, robust picture of the relative strip position offsets between  
1159 layers. The next goal will be to use the cosmics relative local offsets to improve the alignment  
1160 model and better position the sTGC strips in ATLAS.

1161 Muons are important signatures of electroweak and Higgs sector events that physicists an-  
1162 ticipate studying with a high-statistics dataset [3, 5]. An effective alignment model of sTGC  
1163 strip positions will ensure that the NSWs can be used to accomplish the ATLAS collabora-  
1164 tion’s physics goals during the High Luminosity era of the LHC.

# <sup>1165</sup> References

- <sup>1166</sup> [1] L. Evans and P. Bryant. LHC Machine. *Journal of Instrumentation*, 3(S08001), August 2008.
- <sup>1168</sup> [2] G. Apollinari et al. High-Luminosity Large Hadron Collider (HL-LHC) Technical Design Report V. 0.1. Technical Report CERN-2017-007-M, CERN, Geneva, September 2017.
- <sup>1170</sup> [3] A. Dainese et al. The physics potential of HL-LHC. In *Input to the European Particle Physics Strategy Update*, November 2018.
- <sup>1172</sup> [4] The ATLAS Collaboration. The ATLAS Experiment at the CERN Large Hadron Col-  
<sup>1173</sup> linder. *Journal of Instrumentation*, 3(08):S08003, August 2008.
- <sup>1174</sup> [5] T. Kawamoto et al. New Small Wheel Technical Design Report. Technical Report  
<sup>1175</sup> CERN-LHCC-2013-006, ATLAS-TDR-020, CERN, Geneva, June 2013.
- <sup>1176</sup> [6] A. Abusleme et al. Performance of a Full-Size Small-Strip Thin Gap Chamber Prototype  
<sup>1177</sup> for the ATLAS New Small Wheel Muon Upgrade. *Nuclear Instruments and Methods in Physics Research Section A: Accelerators, Spectrometers, Detectors and Associated  
1178 Equipment*, 817:85–92, May 2016. arXiv: 1509.06329.
- <sup>1180</sup> [7] E.M. Carlson. *Results of the 2018 ATLAS sTGC test beam and internal strip alignment  
of sTGC detectors*. M.Sc. thesis, University of Victoria, Victoria, Canada, 2019.
- <sup>1182</sup> [8] B. Lefebvre. Precision survey of the readout strips of small-strip Thin Gap Chambers  
<sup>1183</sup> using X-rays for the muon spectrometer upgrade of the ATLAS experiment. *Journal of  
1184 Instrumentation*, 15(07):C07013–C07013, July 2020.
- <sup>1185</sup> [9] D.J. Griffiths. *Introduction to elementary particles*. Physics textbook. Wiley-VCH,  
<sup>1186</sup> Weinheim, Germany, 2., rev. ed., 5. reprint edition, 2011.
- <sup>1187</sup> [10] M.E. Peskin and D.V. Schroeder. *An introduction to quantum field theory*. Addison-  
<sup>1188</sup> Wesley Pub. Co, Reading, Massachusetts, 1995.

- 1189 [11] P.A. Zyla et al. Review of Particle Physics. *PTEP*, 2020(8):083C01, 2020.
- 1190 [12] M. Kobayashi and T. Maskawa. CP-violation in the renormalizable theory of weak  
1191 interaction. *Progress of theoretical physics*, 49(2):652–657, February 1973.
- 1192 [13] M.L. Perl et al. Evidence for Anomalous Lepton Production in  $\{e\}^{\{+}\backslash\text{ensuremath}{-}\}$   
1193  $\{e\}^{\{\backslash\text{ensuremath}{-}\}}\}$  Annihilation. *Physical Review Letters*, 35(22):1489–1492, De-  
1194 cember 1975. Publisher: American Physical Society.
- 1195 [14] F. Englert and R. Brout. Broken Symmetry and the Mass of Gauge Vector Mesons.  
1196 *Physical Review Letters*, 13(9):321–323, August 1964. Publisher: American Physical  
1197 Society.
- 1198 [15] P.W. Higgs. Broken symmetries, massless particles and gauge fields. *Physics Letters*,  
1199 12(2):132–133, September 1964.
- 1200 [16] D. Galbraith and C. Burgard. UX: Standard Model of the Stan-  
1201 dard Model, November 2013. [http://davidgalbraith.org/portfolio/  
1202 ux-standard-model-of-the-standard-model/](http://davidgalbraith.org/portfolio/ux-standard-model-of-the-standard-model/) last accessed on 2021-09-30.
- 1203 [17] C.A. Bertulani. *Nuclear physics in a nutshell*. In a nutshell. Princeton University Press,  
1204 Princeton, N.J, 2007. OCLC: ocm85690422.
- 1205 [18] B.W. Carroll and D.A. Ostlie. *An introduction to modern astrophysics*. Pearson  
1206 Addison-Wesley, San Francisco, 2nd ed edition, 2007. OCLC: ocm69020924.
- 1207 [19] M. Boezio and E. Mocchiutti. Chemical composition of galactic cosmic rays with space  
1208 experiments. *Astroparticle Physics*, 39-40:95–108, December 2012.
- 1209 [20] The SNO Collaboration. Combined analysis of all three phases of solar neutrino data  
1210 from the sudbury neutrino observatory. *Phys. Rev. C*, 88:025501, August 2013.
- 1211 [21] B. Pontecorvo. Neutrino Experiments and the Problem of Conservation of Leptonic  
1212 Charge. *Soviet Physics—JETP*, 53:1717–1725, 1967.
- 1213 [22] S.M. Bilenky and S.T. Petcov. Massive neutrinos and neutrino oscillations. *Reviews of  
1214 Modern Physics*, 59(3):671–754, July 1987.
- 1215 [23] B. Young. A survey of dark matter and related topics in cosmology. *Frontiers of Physics*,  
1216 12(2):121201, April 2017.
- 1217 [24] C. Muñoz. Dark matter detection in the light of recent experimental results. *International  
1218 Journal of Modern Physics A*, 19(19):3093–3169, July 2004.

- 1219 [25] G. Arnison et al. Experimental observation of isolated large transverse energy elec-  
1220 trons with associated missing energy at s=540 GeV. *Physics Letters B*, 122(1):103–116,  
1221 February 1983.
- 1222 [26] M. Banner et al. Observation of single isolated electrons of high transverse momentum  
1223 in events with missing transverse energy at the CERN pp collider. *Physics Letters B*,  
1224 122(5):476–485, March 1983.
- 1225 [27] G. Arnison et al. Experimental observation of lepton pairs of invariant mass around 95  
1226 GeV/c<sup>2</sup> at the CERN SPS collider. *Physics Letters B*, 126(5):398–410, July 1983.
- 1227 [28] P. Bagnaia et al. Evidence for Z → e<sup>+</sup>e<sup>-</sup> at the CERN pp collider. *Physics Letters B*,  
1228 129(1):130–140, 1983.
- 1229 [29] The CDF Collaboration. Observation of Top Quark Production in  $\bar{p}p$  Collisions with  
1230 the Collider Detector at Fermilab. *Physical Review Letters*, 74(14):2626–2631, April  
1231 1995. Publisher: American Physical Society.
- 1232 [30] The D0 Collaboration. Observation of the Top Quark. *Physical Review Letters*,  
1233 74(14):2632–2637, April 1995. Publisher: American Physical Society.
- 1234 [31] The ATLAS Collaboration. Observation of a new particle in the search for the Standard  
1235 Model Higgs boson with the ATLAS detector at the LHC. *Physics Letters B*, 716(1):1–  
1236 29, September 2012. arXiv: 1207.7214.
- 1237 [32] The CMS Collaboration. Observation of a new boson at a mass of 125 GeV with the  
1238 CMS experiment at the LHC. *Physics Letters B*, 716(1):30–61, September 2012. arXiv:  
1239 1207.7235.
- 1240 [33] Standard Model Summary Plots June 2021, June 2021. <https://atlas.web.cern.ch/Atlas/GROUPS/PHYSICS/PUBNOTES/ATL-PHYS-PUB-2021-032/> last accessed on 2021-  
1241 09-30.
- 1243 [34] O.S. Brüning et al. LHC Design Report. Design Report CERN-2004-003-V-1, CERN,  
1244 CERN, Geneva, Switzerland, 2004. ISBN: 9789290832249.
- 1245 [35] ATLAS luminosity public results run-1, March 2011. <https://twiki.cern.ch/twiki/bin/view/AtlasPublic/LuminosityPublicResults> last accessed on 2021-09-20.
- 1247 [36] ATLAS luminosity public results run-2, July 2015. <https://twiki.cern.ch/twiki/bin/view/AtlasPublic/LuminosityPublicResultsRun2> last accessed on 2021-09-20.

- 1249 [37] The European Strategy for Particle Physics. Technical Report CERN/2685, CERN,  
1250 2006. Adopted by the CERN council at a special session at ministerial level in Lisbon  
1251 in 2006.
- 1252 [38] HiLumi HL-LHC Project. LHC/HL-LHC plan (last update january 2021). <https://hilumilhc.web.cern.ch/content/hl-lhc-project>, last accessed on 2021-09-09.
- 1254 [39] M. Cepeda et al. Report from Working Group 2: Higgs Physics at the HL-LHC and  
1255 HE-LHC. In A. Dainese et al., editors, *Report on the Physics at the HL-LHC, and*  
1256 *Perspectives for the HE-LHC*, number CERN-LPCC-2018-04, pages 221–584. 364 p,  
1257 CERN, Geneva, Switzerland, Jun 2018. CERN.
- 1258 [40] ATLAS inner detector : Technical Design Report, 1. Technical Report CERN-LHCC-  
1259 97-016, CERN, April 1997. ISBN: 9789290831020 Publication Title: CERN Document  
1260 Server.
- 1261 [41] S. Haywood, L. Rossi, R. Nickerson, and A. Romanouk. ATLAS inner detector :  
1262 Technical Design Report, 2. Technical Report CERN-LHCC-97-017, CERN, April 1997.  
1263 ISBN: 9789290831037 Publication Title: CERN Document Server.
- 1264 [42] C. Grupen, B.A. Shwartz, and H. Spieler. *Particle detectors*. Cambridge University  
1265 Press, Cambridge, UK; New York, 2008. OCLC: 1105536566.
- 1266 [43] ATLAS liquid-argon calorimeter : Technical Design Report. Technical Report CERN-  
1267 LHCC-96-041, CERN, 1996. ISBN: 9789290830900 Publication Title: CERN Document  
1268 Server.
- 1269 [44] ATLAS tile calorimeter : Technical Design Report. Technical Report CERN-LHCC-96-  
1270 042, CERN, 1996. ISBN: 9789290830917 Publication Title: CERN Document Server.
- 1271 [45] The ATLAS Collaboration. ATLAS Muon Spectrometer: Technical Design Report.  
1272 Technical Report CERN-LHCC-97-022, CERN, Geneva, 1997.
- 1273 [46] ATLAS magnet system : Technical Design Report, 1. Technical Report CERN-LHCC-  
1274 97-018, CERN, April 1997. ISBN: 9789290831044 Publication Title: CERN Document  
1275 Server.
- 1276 [47] The ATLAS Collaboration. Performance of the ATLAS muon trigger in pp collisions  
1277 at  $\sqrt{s} = 8$  TeV. *The European Physical Journal C*, 75(3):120, March 2015. arXiv:  
1278 1408.3179.

- 1279 [48] S. Aefsky et al. The Optical Alignment System of the ATLAS Muon Spectrometer End-  
1280 caps. *Journal of Instrumentation*, 3(11):P11005–P11005, November 2008. Publisher:  
1281 IOP Publishing.
- 1282 [49] ATLAS level-1 trigger : Technical Design Report. Technical Report CERN-LHCC-98-  
1283 014, CERN, August 1998. ISBN: 9789290831280 Publication Title: CERN Document  
1284 Server.
- 1285 [50] A. Ruiz Martínez. The run-2 ATLAS trigger system. *Journal of Physics: Conference  
1286 Series*, 762:012003, October 2016.
- 1287 [51] Technical Design Report for the Phase-II Upgrade of the ATLAS TDAQ System. Tech-  
1288 nical Report CERN-LHCC-2017-020, ATLAS-TDR-029, CERN, Geneva, September  
1289 2017.
- 1290 [52] P. Jenni, M. Nessi, M. Nordberg, and K. Smith. ATLAS high-level trigger, data-  
1291 acquisition and controls : Technical Design Report. Technical Report CERN-LHCC-  
1292 2003-022, CERN, July 2003.
- 1293 [53] E. Perez Codina. Small-strip Thin Gap Chambers for the muon spectrometer upgrade of  
1294 the ATLAS experiment. *Nuclear Instruments and Methods in Physics Research Section  
1295 A: Accelerators, Spectrometers, Detectors and Associated Equipment*, 824:559–561, July  
1296 2016.
- 1297 [54] J. Townsend. *Electricity in gases*. Clarendon Press, Oxford, 1915.
- 1298 [55] S. Majewski, G. Charpak, A. Breskin, and G. Mikenberg. A thin multiwire chamber  
1299 operating in the high multiplication mode. *Nuclear Instruments and Methods*, 217:265–  
1300 271, 1983.
- 1301 [56] E. Gatti, A. Longoni, H. Okuno, and P. Semenza. Optimum geometry for strip cathodes  
1302 or grids in MWPC for avalanche localization along the anode wires. *Nuclear Instruments  
1303 and Methods*, 163(1):83–92, July 1979.
- 1304 [57] G. Battistoni et al. Resistive cathode transparency. *Nuclear Instruments and Methods  
1305 in Physics Research*, 202(3):459–464, November 1982.
- 1306 [58] B. Lefebvre. *Characterization studies of small-strip Thin Gap Chambers for the ATLAS  
1307 Upgrade*. PhD thesis, McGill University, Montreal, Canada, 2018.
- 1308 [59] P.K.F. Grieder. *Cosmic rays at Earth: researcher’s reference manual and data book*.  
1309 Elsevier Science Ltd, Amsterdam, 1st ed edition, 2001.

- 1310 [60] R. Keyes et al. Development and characterization of a gas system and its associated  
 1311 slow-control system for an ATLAS small-strip thin gap chamber testing facility. *Journal*  
 1312 *of Instrumentation*, 12(04):P04027–P04027, April 2017.
- 1313 [61] Georgios Iakovidis. VMM3, an ASIC for Micropattern Detectors. Technical Report  
 1314 ATL-MUON-PROC-2018-003, CERN, Geneva, March 2018.
- 1315 [62] B. Chen. *Calibration Studies of the Front-End Electronics for the ATLAS New Small*  
 1316 *Wheel Project*. M.Sc. thesis, McGill University, Montreal, Canada, 2019.
- 1317 [63] R. Brun and F. Rademakers. ROOT: An object oriented data analysis framework. *Nu-*  
 1318 *clear Instruments and Methods in Physics Research Section A: Accelerators, Spectrome-*  
 1319 *ters, Detectors and Associated Equipment*, 389:81–86, 1997. See also ”ROOT” [software],  
 1320 Release 6.18/02, 23/08/2019, (<https://zenodo.org/record/3895860#.YVJW6n0pCHs>).
- 1321 [64] F. Sauli. Principles of operation of multiwire proportional and drift chambers. Number 81 in CERN Academic Training Lectures, CERN, Geneva, Switzerland, September  
 1322 1975 – June 1976. CERN.
- 1323 [65] M. Hatlo et al. Developments of mathematical software libraries for the LHC experi-  
 1324 ments. *IEEE Transactions on Nuclear Science*, 52:2818–2822, 2005.
- 1325 [66] H. Guo. A Simple Algorithm for Fitting a Gaussian Function [DSP Tips and Tricks].  
 1326 *IEEE Signal Processing Magazine*, 28(5):134–137, September 2011.
- 1327 [67] I. Endo et al. Systematic shifts of evaluated charge centroid for the cathode read-out  
 1328 multiwire proportional chamber. *Nuclear Instruments and Methods in Physics Research*,  
 1329 188(1):51–58, September 1981.
- 1330 [68] Minature x-ray source mini-x. Product of Amptek Inc. <https://www.amptek.com/-/media/ametekamptek/documents/resources/specs/mini-x-specifications.pdf?la=en&revision=512f7eb3-01b3-47fd-864f-5525c850fc6e&hash=B8B03C0592486E2D91C566C4326F15F5>, last accessed on 2021-10-15.
- 1331 [69] B. Stelzer. The New Small Wheel Upgrade Project of the ATLAS Experiment. *Nuclear*  
 1332 *and Particle Physics Proceedings*, 273-275:1160–1165, April 2016.
- 1333 [70] X. Zhao et al. Cosmic test of sTGC detector prototype made in China for ATLAS  
 1334 experiment upgrade. *Nuclear Instruments and Methods in Physics Research Section A:*  
 1335 *Accelerators, Spectrometers, Detectors and Associated Equipment*, 927:257–261, May  
 1336 2019.

<sup>1341</sup> APPENDICES

<sub>1342</sub> **Appendix A**

<sub>1343</sub> **Uncertainty in cluster positions**

<sub>1344</sub> The clusters were fit with Guo's method [66] and Minuit2 for ROOT [65]. The difference in  
<sub>1345</sub> cluster means between the two algorithms is shown in figure A.1.

<sub>1346</sub> The RMS of the distribution in figure A.1 is 57  $\mu\text{m}$ , which is much larger than the statistical  
<sub>1347</sub> uncertainty in the mean for the Minuit2 algorithm, which peaks around 7  $\mu\text{m}$ . An RMS of  
<sub>1348</sub> 60  $\mu\text{m}$  is common for data taken with most quadruplets at 3.1 kV. Therefore, the uncer-  
<sub>1349</sub> tainty in the reconstructed cluster  $y$ -coordinate is assigned 60  $\mu\text{m}$  due to variations in the  
<sub>1350</sub> reconstruction with different Gaussian fit algorithms.

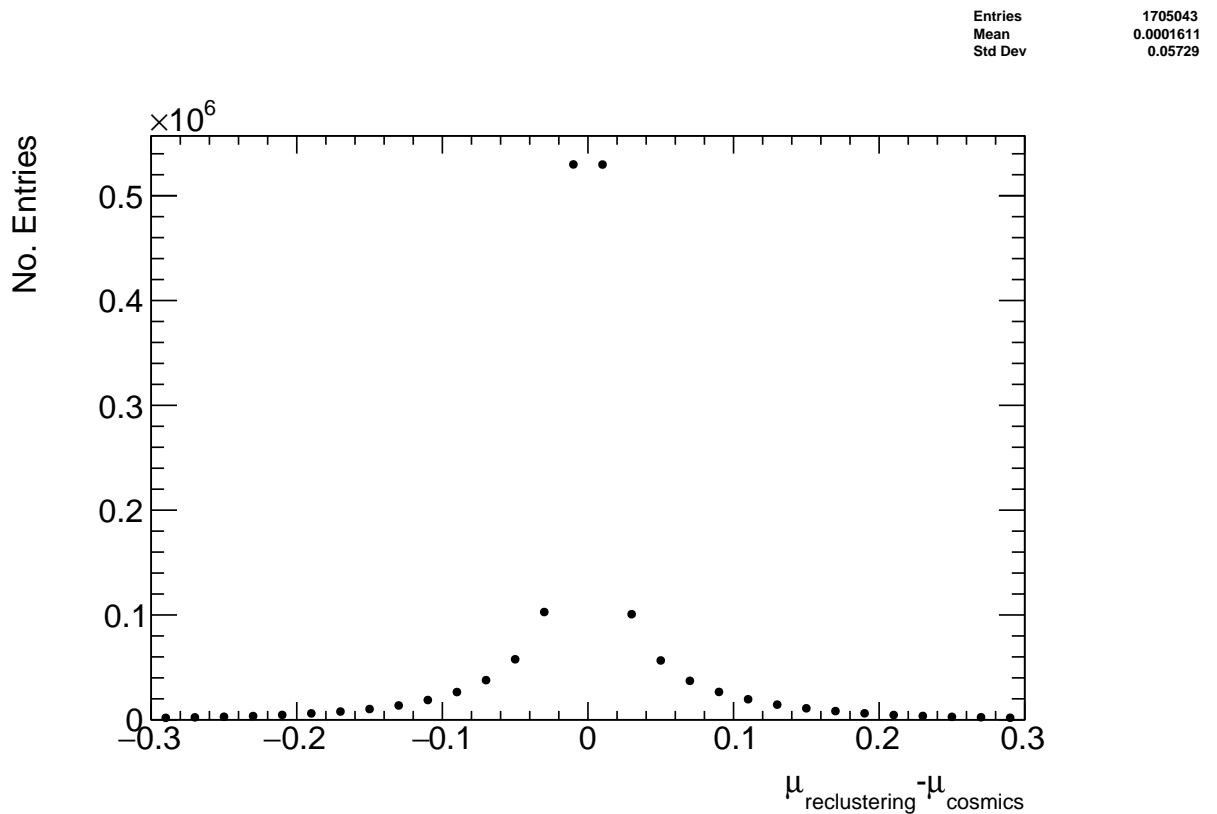


Figure A.1: The difference between cluster means calculated with Guo's method [66] in `tgc_analysis/CosmicsAnalysis` and Minuit2 for ROOT [65] in `strip_position_analysis/ReClustering` for data collected with QL2.P.8 at 3.1 kV.

<sub>1351</sub> **Appendix B**

<sub>1352</sub> **Study of cosmics for alignment  
analysis statistical uncertainty**

<sub>1354</sub> Typically, one million triggers (cosmic muon events, noise, photons and  $\delta$ -rays) were collected  
<sub>1355</sub> for each Canadian quadruplet at McGill University, resulting in roughly half the number of  
<sub>1356</sub> viable tracks after cuts. For QS3.P.18, 3.5 million triggers were collected. To gauge the  
<sub>1357</sub> sensitivity of the analysis to the available statistics, partitions of this data with each with  
<sub>1358</sub> a different number of triggers were analyzed separately. Ultimately, the quantity of interest  
<sub>1359</sub> was the Gaussian mean of the residual distribution in regions of interest, so the peak in the  
<sub>1360</sub> distribution of the statistical uncertainty in the residual means for each area of interest for  
<sub>1361</sub> a specific tracking combination was used to gauge the quality of the analysis. How the peak  
<sub>1362</sub> in the residual mean uncertainty distribution changes with the number of triggers is shown  
<sub>1363</sub> in figure for tracks on layer 1 built from layers 3 and 4 [B.1](#).

<sub>1364</sub> The uncertainty is already around 20  $\mu\text{m}$  at 1 million triggers, suitable for distinguishing  
<sub>1365</sub> differences in offsets of order 50  $\mu\text{m}$  as required. Although increased statistics could decrease  
<sub>1366</sub> the statistical uncertainty, it is not required for the goals of this analysis. Moreoever, the  
<sub>1367</sub> systematic uncertainty on the mean cosmics residuals is around 50  $\mu\text{m}$  so the statistical  
<sub>1368</sub> uncertainty of 20  $\mu\text{m}$  is nearly negligible.

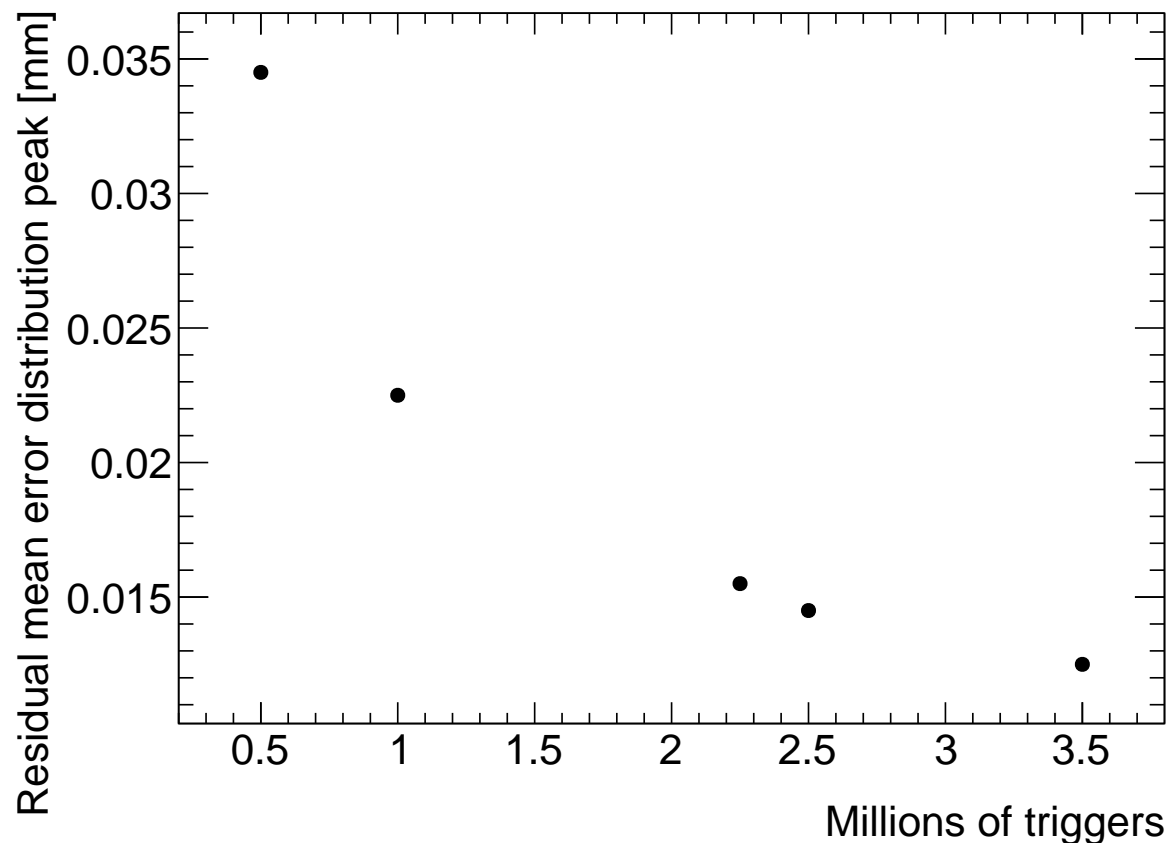


Figure B.1: How the peak of the distributions of uncertainties in the residual means in regions of interest for tracks on layer 1 built from layers 3 and 4 changed with the number of triggers used in the analysis. The distribution falls off as  $\frac{1}{\sqrt{N}}$  as expected.

# <sup>1369</sup> Appendix C

## <sup>1370</sup> Study of systematic uncertainties <sup>1371</sup> when using cosmics data for <sup>1372</sup> alignment studies

### <sup>1373</sup> C.1 Residual distribution fit function

<sup>1374</sup> The distribution of residuals should be modeled by a double Gaussian fit[58]:

$$G(r) = A_s \exp\left[\frac{-(r - \mu)^2}{2\sigma_s^2}\right] + A_b \exp\left[\frac{-(r - \mu)^2}{2\sigma_b^2}\right] \quad (\text{C.1})$$

<sup>1375</sup> where  $r$  is the residual,  $A$  is the Gaussian amplitude,  $\mu$  is the Gaussian mean,  $\sigma$  is the  
<sup>1376</sup> Gaussian sigma, and the subscripts  $s$  and  $b$  stand for signal and background respectively.  
<sup>1377</sup> One Gaussian captures the real (signal) tracks and the other captures the tracks built from  
<sup>1378</sup> noise (background). The Gaussian with the smaller width is identified as the signal.

<sup>1379</sup> A single Gaussian fit failed less often than a double Gaussian fit. The Gaussian fits were  
<sup>1380</sup> performed by initially estimating the amplitude to be 100 tracks, the Gaussian mean to be  
<sup>1381</sup> the histogram mean, and Gaussian  $\sigma$  to be the RMS. The fit range was restricted to  $\pm 1$   
<sup>1382</sup> root-mean-square (RMS) from the histogram mean. The modification helped the Gaussian  
<sup>1383</sup> fit capture the signal peak. An example residual distribution is shown in figure C.1.

<sup>1384</sup> For all residual distributions in 100 mm by 100 mm bins on layer 4 built from clusters on  
<sup>1385</sup> layers 1 and 2, the difference in Gaussian and double Gaussian means and  $\sigma$ 's is shown in  
<sup>1386</sup> figure C.2a. The mean of the distribution is centered around zero (within the RMS of the

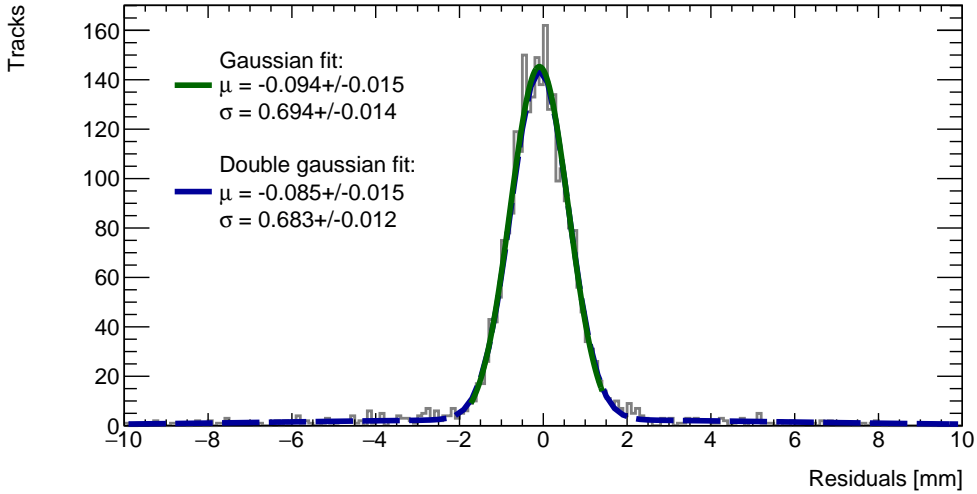
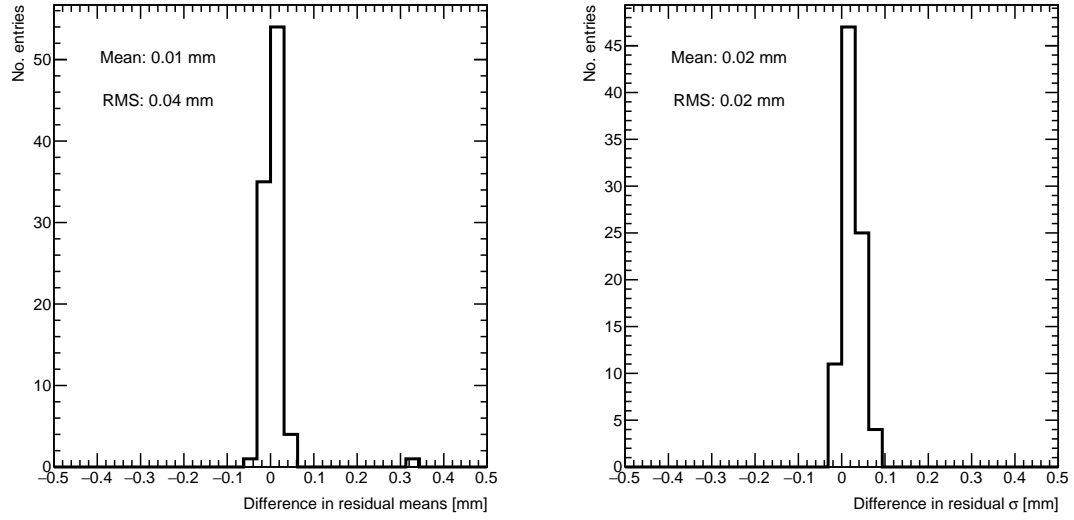


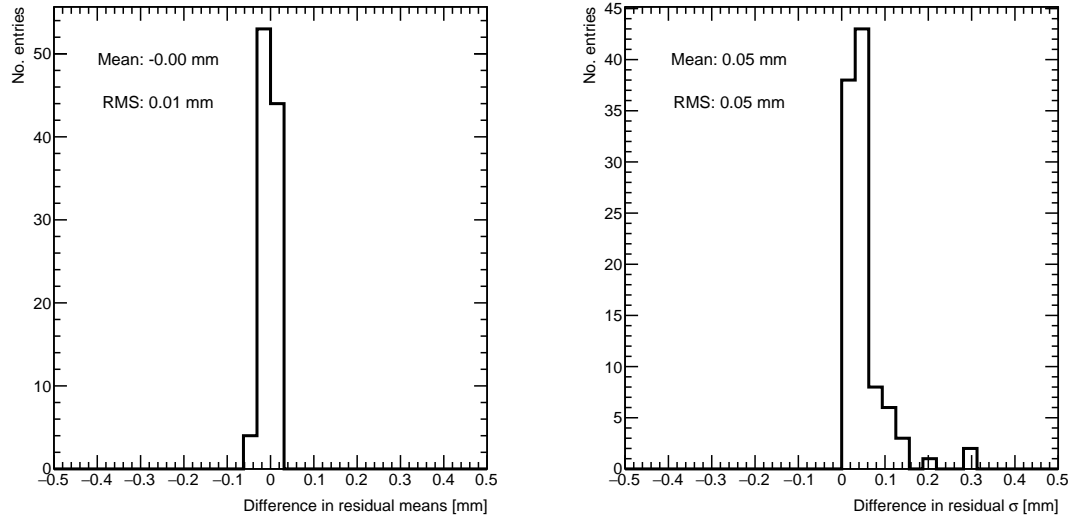
Figure C.1: Residual distribution for track residuals on layer 4 built from clusters on layers 1 and 2 for  $x \in [-3.00, 97.00]$  mm,  $y \in [394.60, 494.60]$  mm, fit with a double Gaussian and a single Gaussian in a range of  $\pm 1$  RMS from the histogram mean.

1387 distribution) so the choice of fit algorithm imbues no measurable bias. The order of the  
1388 RMS is such that the difference in residual means at 40  $\mu\text{m}$  is just significant, so it should  
1389 be accounted for as a systematic uncertainty on the Gaussian residual means. The 40  $\mu\text{m}$   
1390 RMS is for the tracking combination with the worst extrapolation lever arm and the widest  
1391 distribution of mean differences; the interpolation combinations have narrower distributions,  
1392 as shown in figure C.2b. The RMS of the distribution for residual means on layer 2 obtained  
1393 using reference layers 1 and 3 is only 10  $\mu\text{m}$ , which is almost negligible.

1394 The Gaussian  $\sigma$  should be larger than the double Gaussian  $\sigma$  because the Gaussian distri-  
1395 bution includes the effect of the noise tracks that can yield large residuals, while the double  
1396 Gaussian models signal and background residuals separately. For this analysis, only the  
1397 residual mean was important, so the systematic overestimate of the signal  $\sigma$  in the Gaussian  
1398 fit shown in the right-side plots of figure C.2 was allowed.



(a) Difference in residual distribution means (left) and  $\sigma$ 's (right) extracted with a Gaussian and double Gaussian fit, for all residual distributions in 100 mm by 100 mm bins on layer 4 built from clusters on layers 1 and 2 for sample quadruplet QL2.P.8.



(b) Difference in residual distribution means (left) and  $\sigma$ 's (right) for a Gaussian and double Gaussian fit, for all residual distributions in 100 mm by 100 mm bins on layer 2 built from clusters on layers 1 and 3 for sample quadruplet QL2.P.8.

Figure C.2

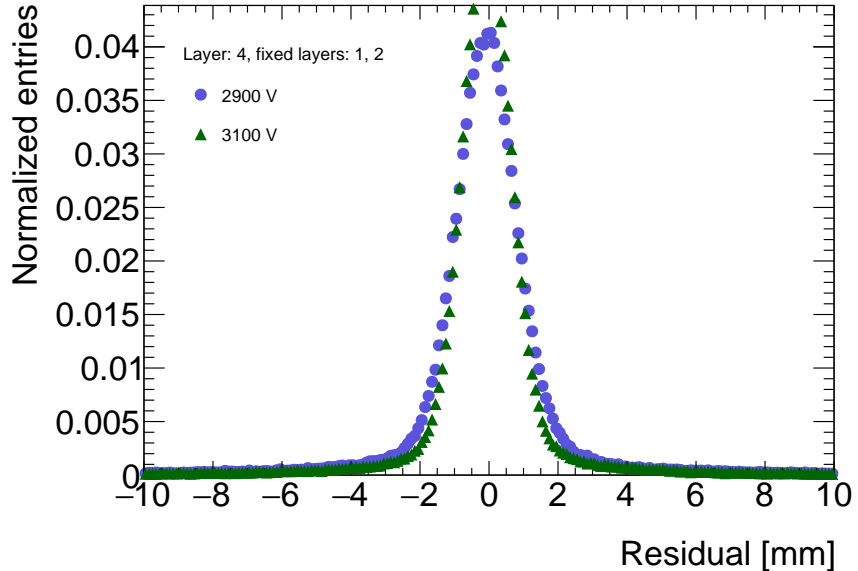


Figure C.3: Residual distribution for tracks on layer 4 built from clusters on layers 1 and 2 for sample quadruplet QL2.P.8 for data collected at 2.9 kV and 3.1 kV.

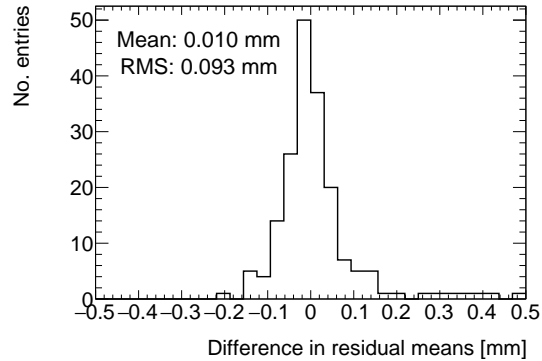
<sup>1399</sup> Ultimately, a Gaussian fit was chosen for the track residual distributions because it was more  
<sup>1400</sup> robust and did not affect the fitted mean values too strongly.

## <sup>1401</sup> C.2 Cosmic muon data collection voltage

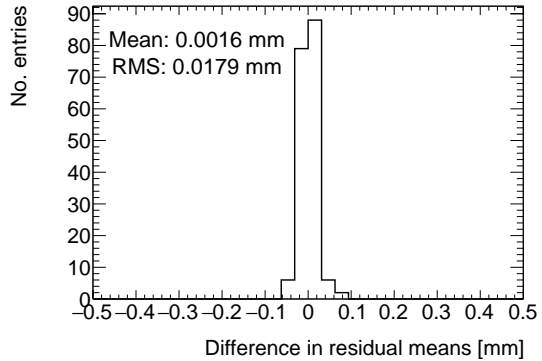
<sup>1402</sup> Cosmic muon data was collected at 2.9 kV and 3.1 kV because although 2.9 kV is closer to  
<sup>1403</sup> the operating conditions the chambers will be subject to in ATLAS, the extra gain provided  
<sup>1404</sup> by operating at 3.1 kV increased the signal to noise ratio for pad signals. Also, the tracking  
<sup>1405</sup> efficiency was higher with data collected at 3.1 kV. As such, cosmic muon data collected at  
<sup>1406</sup> 3.1 kV was used in the analysis presented in the body of the thesis.

<sup>1407</sup> The difference in gain affects the relative population of clusters of different sizes, which in  
<sup>1408</sup> turn affects the uncertainty in the mean cluster positions on each layer, the uncertainty in  
<sup>1409</sup> the track positions and the residual distributions. The residual distributions for 3.1 kV data  
<sup>1410</sup> are narrower, as shown in figure C.3.

<sup>1411</sup> Neither dataset is better for calculating the mean of residuals in a given area, so a systematic  
<sup>1412</sup> uncertainty can be assigned based on the difference in residual means calculated for 2.9 kV  
<sup>1413</sup> and 3.1 kV data per tracking combination. For each tracking combination, the difference



(a) Difference in residual means when measured with residuals on layer 4 built from clusters on layers 1 and 2.



(b) Difference in residual means when measured with residuals on layer 2 built from clusters on layers 1 and 3.

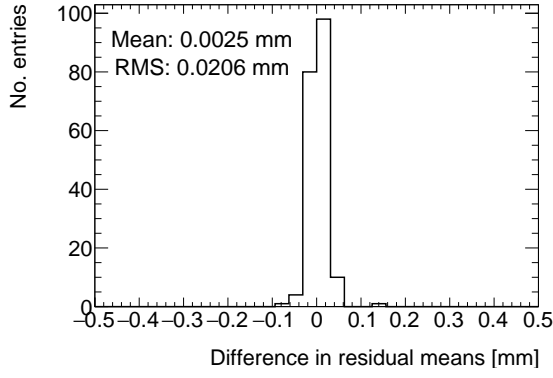
Figure C.4: Difference in residual means for data collected with sample quadruplet QL2.P.8 at 2.9 kV and 3.1 kV respectively in 100 mm by 100 mm bins.

in the fitted track residual means in 100 mm by 100 mm areas for 2.9 kV and 3.1 kV data are put in a distribution for a sample quadruplet, as shown in figure C.4. The means of the distributions for both tracking combinations are near zero, so as expected the collection voltage introduces no bias. Tracks built from clusters on layers 1 and 2 and extrapolated to layer 4 have the worst lever arm and hence the largest root-mean-square (RMS) of 100  $\mu\text{m}$ . The width of the distributions for geometrically favourable tracking combinations are much narrower. The narrowest width of the residual mean difference distribution is for tracks on layer 2 built from clusters on layers 1 and 3 (see figure C.4b), with a value of 20  $\mu\text{m}$ .

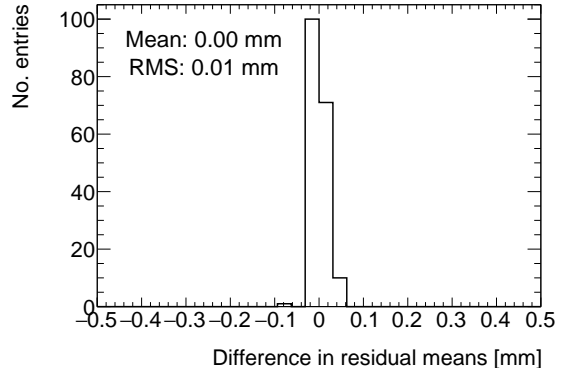
### C.3 Cluster fit algorithm

To ensure that changing the cluster fitting algorithm like in appendix A would not change the calculated mean of residuals in each region of interest significantly, the residual means were compared in both cases. The distribution of the difference in residual means is plotted in figure C.5 for the tracking combinations with the worst and most favourable extrapolation lever arms.

The mean of the distributions are centered around zero, so the choice of cluster fit algorithm did not introduce any bias. Differences on the order of 50  $\mu\text{m}$  are important, so the root-mean-squares (RMS's) of the distributions show that the clustering algorithm had a small but notable effect between 10-20  $\mu\text{m}$  from the most to least geometrically favourable tracking



(a) Difference in residual means when measured with residuals on layer 4 built from clusters on layers 1 and 2.



(b) Difference in residual means when measured with residuals on layer 2 built from clusters on layers 1 and 3.

Figure C.5: Difference in residual means when the cluster fit algorithm is `Minuit2` [65] versus Guo's method [66] for two different tracking combinations for sample quadruplet, QL2.P.8.

combinations. Therefore, the RMS for each tracking combination will be used to add a systematic uncertainty on the residual means accounting for the effect that different cluster fit algorithms have on the residual means.

## C.4 Differential non-linearity

### Definition

In this context, differential non-linearity (DNL) is when the reconstructed cluster mean is biased by the fit of the discretely sampled peak signal amplitude distribution over the strips. The bias depends on the relative position of the avalanche with respect to the center of the closest strip. For a summary of DNL, refer to page 40 of [58], an early paper studying its effects [67], and for an example application, refer to [6].

### Application and effect of DNL

The cluster mean was corrected for DNL using the equation:

$$y' = y + a \sin(2\pi y_{rel}) \quad (\text{C.2})$$

where  $y$  is the cluster mean,  $y_{rel}$  is the relative position of the cluster mean with respect to the strip's center,  $a$  is the amplitude of the correction, and  $y'$  is the corrected cluster

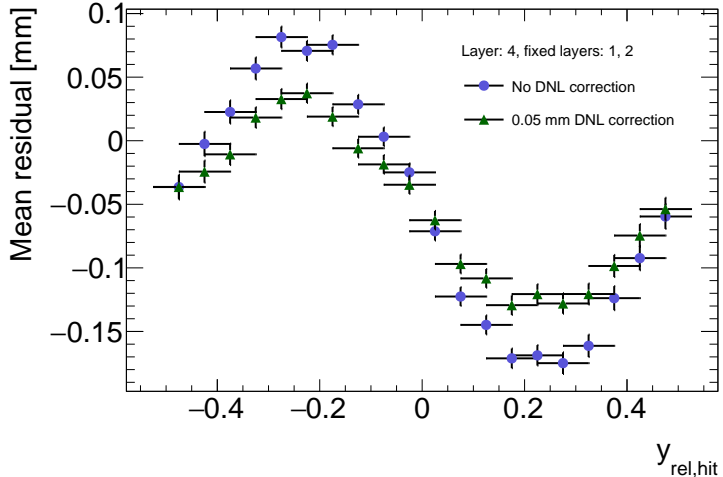


Figure C.6: Effect applying a  $50 \mu\text{m}$  DNL correction to the profile of the residuals sorted by  $y_{rel}$  for residuals built from clusters on layers 1 and 2 and extrapolated to layer 4 of quadruplet, QL2.P.8.

mean. The amplitude can be derived by comparing the reconstructed hit position to the expected hit position, as done in [6]. With cosmic muons, there is no reference hit position to compare to, so track residuals were used as a proxy [58]. The hallmark of the DNL effect is the periodic pattern in the residual versus  $y_{rel}$  profile, and the effect of correcting the cluster means using an amplitude of  $50 \mu\text{m}$  is shown in figure C.6. An amplitude of  $50 \mu\text{m}$  is based on Dr. Lefebvre's [58] estimate of the DNL amplitudes by layer, quadruplet and cluster size using cosmic muon tracks [58]. Little variation is seen in the amplitude parameters with respect to the quadruplet tested, the layer and the cluster size so a universal correction is used.

Although the correction is not large enough in this case, the figure shows that the correction does reduce the DNL effect. Slightly better performance is seen in the interpolation tracking combinations where the quality of the residuals is better. DNL corrections for cosmic muon data are difficult because the DNL effect is obscured by the effect of misalignments between strip layers and noise. Misalignments cause the center of the sinusoidal pattern in figure C.6 to be shifted off of zero, since the mean of residuals is shifted.

Figure C.7 shows the distribution of the difference in residual means calculated in  $100 \text{ mm}$  by  $100 \text{ mm}$  areas for mean track residuals on layer 4 obtained using layers 1 and 2 as reference. The mean of the distribution is zero within the root-mean-square so the DNL correction does not bias the residual means. It is apparent that the effect of the DNL correction on

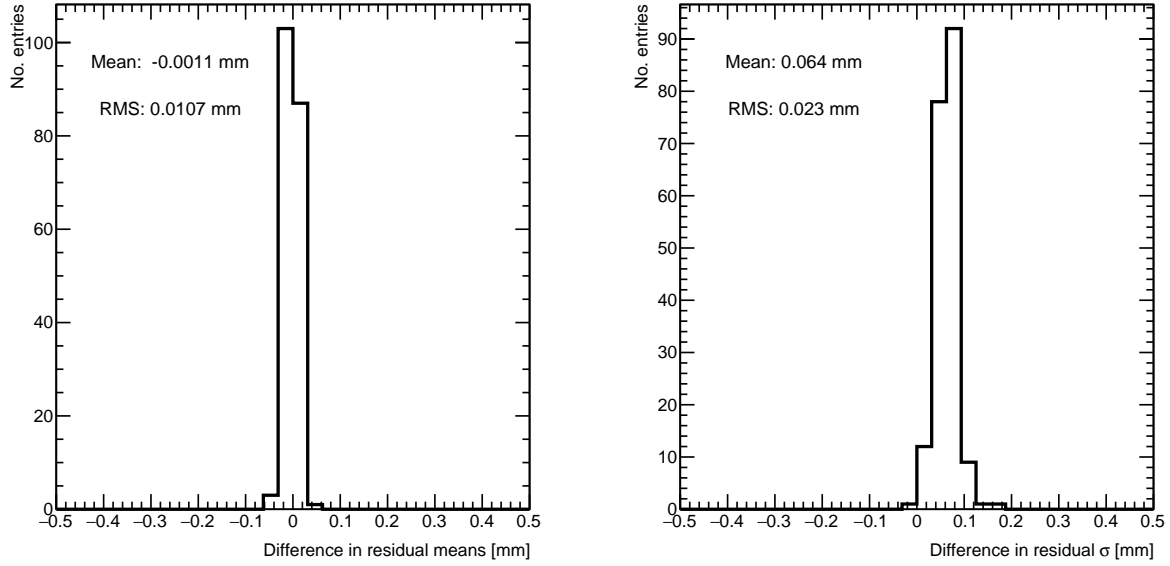


Figure C.7: Difference in residual distribution means and  $\sigma$ 's with and without DNL correction for residuals on layer 4 obtained using reference layers 1 and 2 for sample quadruplet, QL2.P.8.

the residual means is on the order of micrometers given the RMS of  $10 \mu\text{m}$  in the worst extrapolation case. Although the  $\sigma$ 's of the residual distributions shrink with the DNL correction, the mean is the parameter of interest so the bias in the fitted  $\sigma$ 's was ignored. Therefore, in this analysis DNL is not corrected for.

<sub>1469</sub> Appendix D

<sub>1470</sub> Printable plots

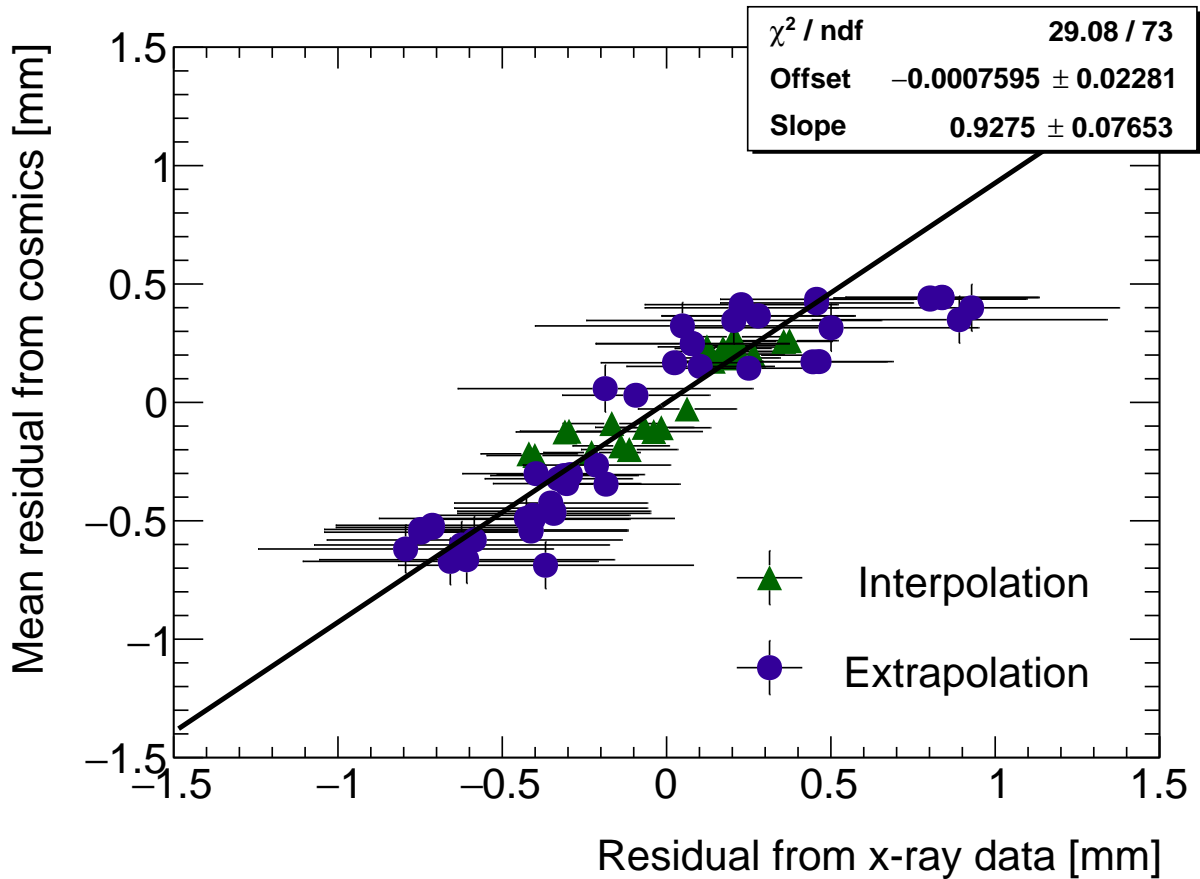


Figure D.1: Correlation plot between x-ray and cosmics residuals for all tracking combinations for QL2.P.11. Each rectangle is centered on an x-ray and mean cosmics residual pair. The width of the rectangles in  $x$  and  $y$  are the uncertainty in the x-ray and mean cosmics residual respectively. This is a printable version of figure 7.2 in section 7.1.

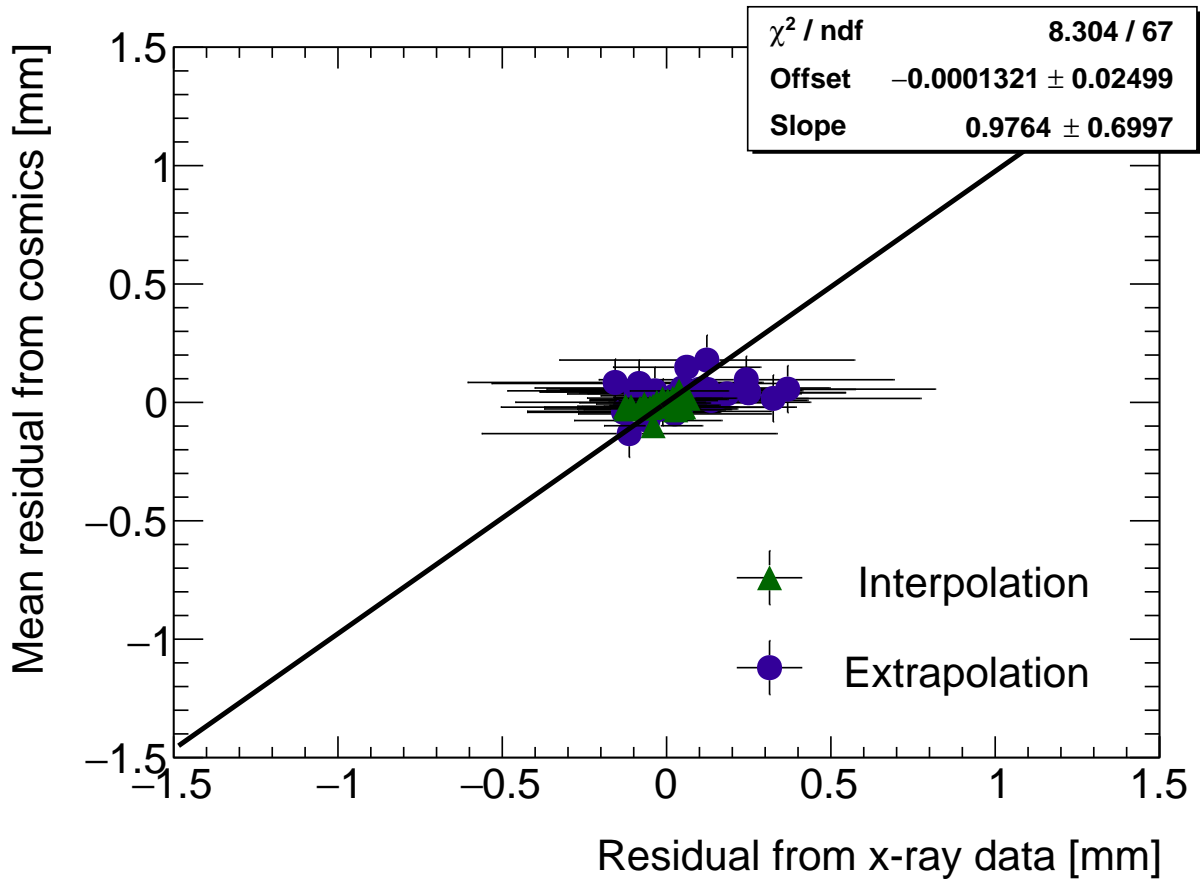


Figure D.2: Correlation plot between x-ray and cosmics residuals for all tracking combinations for QL2.P.8. Each rectangle is centered on an x-ray and mean cosmics residual pair. The width of the rectangles in  $x$  and  $y$  are the uncertainty in the x-ray and mean cosmics residual respectively. This is a printable version of figure 7.3 in section 7.1.